Thermodynamic properties of an $S = \frac{1}{2}$ ring-exchange model on the triangular lattice

Kazuhiro Seki[1] and Seiji Yunoki[1,2,3]
[1]Computational Quantum Matter Research Team, RIKEN, Center for Emergent Matter Science (CEMS), Saitama 351-0198, Japan
[2]Computational Condensed Matter Physics Laboratory, RIKEN Cluster for Pioneering Research (CPR), Saitama 351-0198, Japan
[3]Computational Materials Science Research Team, RIKEN Center for Computational Science (R-CCS), Hyogo 650-0047, Japan

(Received 18 December 2019; accepted 26 May 2020; published 3 June 2020)

By using a numerically exact diagonalization technique and a block-extended version of the finite-temperature Lanczos method, we study thermodynamic properties of an $S = 1/2$ Heisenberg model on the triangular lattice with an antiferromagnetic nearest-neighbor interaction J and a four-spin ring-exchange interaction J_c. Calculations are performed on small clusters under the periodic-boundary conditions. In contrast to the purely triangular case with $J_c = 0$, the specific heat exhibits a characteristic double-peak structure for $J_c/J \gtrsim 0.04$. From the calculations of the entropy and the uniform magnetic susceptibility, it is shown that nonmagnetic excitations exist below the magnetic excitation for $J_c/J \gtrsim 0.04$.

DOI: 10.1103/PhysRevB.101.235115

I. INTRODUCTION

The $S = 1/2$ Heisenberg antiferromagnet on the triangular lattice is a prototypical frustrated quantum system and has been a candidate of a resonating-valence-bond (RVB) or a spin-liquid ground state [1,2]. Although the ground state is likely to be the conventional 120° Néel state according to the recent numerical and theoretical studies [3–8], the quest for a spin-liquid state in the same lattice is still continuing by incorporating additional terms to stabilize a spin-liquid state, such as the next-nearest-neighbor exchange interaction [9–13] and the four-spin ring-exchange interaction J_c [5,14–16]. These exchange interactions can be considered as an introduction of the charge fluctuation [17,18] and thus become more relevant for describing magnetic properties of Mott insulators in proximity of the metal-insulator transition [19–29]. While the ring-exchange interaction itself has long been considered for describing the magnetism in the three-dimensional solid ^{3}He [30–36], NiS$_2$ [37], and the parent compounds of high-T_c cuprate superconductor such as La$_2$CuO$_4$ [38–43], its importance in triangular-lattice systems near the Mott transition is attracting renewed attention recently [15,16,44,45] in organic Mott insulators κ-(ET)$_2$Cu$_2$(CN)$_3$ [46–48] and EtMe$_3$Sb[Pd(dmit)$_2$]$_2$ [49,50] and a charge-density-wave Mott insulator 1T-TaS$_2$ [51,52].

As an effective model for the triangular-lattice materials near the Mott transition but with frozen charge degrees of freedom, the ring-exchange model on the triangular lattice has been proposed [15,16,44,45]. The model is described by the following Hamiltonian:

$$\hat{H} = J\sum_{\langle ij\rangle} \hat{\mathbf{S}}_i \cdot \hat{\mathbf{S}}_j + J_c \sum_{\langle ijkl\rangle} (\hat{P}_{ijkl} + \hat{P}^\dagger_{ijkl}), \tag{1}$$

where J is the nearest-neighbor exchange coupling, J_c is the four-spin ring-exchange coupling, $\hat{\mathbf{S}}_i = (\hat{S}^x_i, \hat{S}^y_i, \hat{S}^z_i)$ is the spin $S = 1/2$ operator, and $\hat{P}_{ijkl}$ permutes four spins at sites i, j, k, and l on an elementary parallelogram cyclically connected as i-j-k-l-i (see Fig. 1). More specifically, we define that i-k and j-l are diagonals of the parallelogram, and k is the next-nearest neighbor of i on the triangular lattice, as indicated in Fig. 1. The ring-exchange operator $\hat{P}_{ijkl}$ can be expressed by a product of permutation operators as

$$\hat{P}_{ijkl} = \hat{P}_{il}\hat{P}_{ik}\hat{P}_{ij}, \tag{2}$$

where $\hat{P}_{ij} = \hat{P}^\dagger_{ij} = 2\hat{\mathbf{S}}_i \cdot \hat{\mathbf{S}}_j + \frac{1}{2}$ is the permutation operator exchanging spins at site i and j. It follows that $\hat{P}^\dagger_{ijkl} = \hat{P}_{lkji} = \hat{P}^{-1}_{ijkl}$. The sum indicated by $\langle ij\rangle$ in the first term of $\hat{H}$ runs over all pairs of nearest-neighbor sites i and j, and the second sum indicated by $\langle ijkl\rangle$ runs over all elementary parallelograms (denoted by shaded blue in Fig. 1) formed by sites i, j, k, and l.

In terms of the t/U expansion of the half-filled Hubbard model with the nearest-neighbor hopping t and the on-site interaction U, the ring-exchange term appears in the fourth-order expansion with $J_c = 20t^4/U^3$, although there are additional correction terms in the expansion with the fourth order [17,18]. Note that the Hamiltonian in Eq. (1) has been considered as a model for the nuclear magnetism of a ^{3}He film adsorbed on graphite preplated with ^{4}He at a particular commensurate density but with a ferromagnetic $J < 0$ [5,53–62], although a recent fixed-node diffusion Monte Carlo calculation poses a question on the realization of such a commensurate crystalline state [63].

Since $J > 0$ and $J_c \geqslant 0$ are relevant for the magnetism near Mott transition, let us briefly summarize the ground-state phase diagram of the model in Eq. (1) for $J > 0$ and $J_c \geqslant 0$ discussed in the previous literature. For $J > 0$ and $J_c = 0$, the ground state is the three-sublattice (120°) Néel ordered state [3–8,15]. For $J = 0$ and $J_c > 0$, the ground state is a spin-liquid state (SL-I), which corresponds to the RVB state, with no spin gap [5,60,64]. Another spin-liquid state (SL-II)

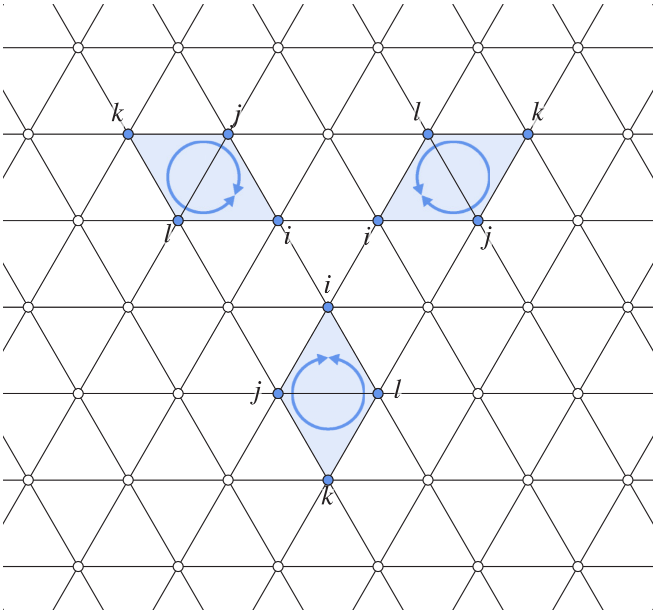

FIG. 1. Schematic of the model described in Eq. (1) on the triangular lattice. Elementary parallelograms, where $\hat{P}_{ijkl}$ and $\hat{P}^{\dagger}_{ijkl}$ act (indicated by circular arrows), are indicated.

appears for moderate J_c/J [5,15,60,64], where the SL-II phase has many singlet excitations in the spin gap (i.e., below the lowest magnetic excitation).

Besides exploring the spin-liquid ground states, it is also crucial to study excitation properties such as thermodynamics as they can be measured experimentally [48,65–67]. In this paper, we examine the effect of the ring-exchange interaction on the thermodynamic properties such as the specific heat, entropy, uniform magnetic susceptibility, and generalized Wilson ratio. Recently, these thermodynamic properties, except for the specific heat, of a model similar to Eq. (1) but without the terms corresponding to Eq. (B4) on a 28-site cluster has been reported [68] using an improved version [69] of the finite-temperature Lanczos method [70–72]. Here, we propose an extended version of the finite-temperature Lanczos method with the block Lanczos algorithm and adopt it for small-cluster calculations up to 36 sites. The block-Lanczos extension allows for an efficient sampling over random states that is required for approximate evaluation of the trace over a basis set of the Hilbert space.

The rest of this paper is organized as follows. The finite-temperature Lanczos method with the extension to the block-Lanczos algorithm is described in Sec. II. The method is applied in Sec. III to calculate the entropy, the specific heat, the uniform magnetic susceptibility, and the generalized Wilson ratio of the model for various values of J_c/J. The results are summarized and discussed in Sec. IV. An algorithm to find a spin configuration from a given state label in a Hilbert space of a fixed magnetization $S^z = \sum_i S_i^z$ is described in Appendix A. The effect of the ring-exchange interaction J_c on the spin-wave excitation in the 120° Néel ordered state is studied within the linear spin-wave theory in Appendix B. Throughout the paper, we set $\hbar = k_B = 1$.

II. METHOD

In this section, we describe the finite-temperature Lanczos method, which allows us to evaluate the partition function and thermal averages of physical observables approximately, without full numerical diagonalization of the Hamiltonian. Before entering the details, let us first briefly summarize the procedure of the finite-temperature Lanczos method. The key approximations made in the finite-temperature Lanczos method are (i) stochastic evaluation of the trace of operator $\hat{O}$ and (ii) approximate evaluation of Boltzmann factor $e^{-\beta\hat{H}}$ by the Lanczos method, where β is the inverse temperature. We use the random-phase states for stochastic samplings in (i) and adopt the block Lanczos method for (ii).

A. Exact partition function

The partition function Z at temperature $T = 1/\beta$ is defined by

$$Z = \mathrm{Tr}[e^{-\beta\hat{H}}] = \sum_{n=1}^{N_{\mathrm{st}}} e^{-\beta E_n}, \tag{3}$$

where E_n is an eigenvalue of $\hat{H}$ associated with an eigenstate $|E_n\rangle$, i.e.,

$$\hat{H}|E_n\rangle = E_n|E_n\rangle, \tag{4}$$

and N_{st} is the number of eigenstates. The thermal average of operator $\hat{A}$ is given by

$$\langle\hat{A}\rangle = \frac{1}{Z}\mathrm{Tr}[e^{-\beta\hat{H}}\hat{A}] = \frac{1}{Z}\mathrm{Tr}[e^{-\beta\hat{H}/2}\hat{A}e^{-\beta\hat{H}/2}]. \tag{5}$$

In practice, one can make use of symmetries of the Hamiltonian to reduce the computational cost for numerical diagonalization or Lanczos iterations as

$$Z = \sum_{\alpha=1}^{N_{\mathrm{sym}}} Z^{(\alpha)} \tag{6}$$

with

$$Z^{(\alpha)} = \sum_{n=1}^{N_{\mathrm{st}}^{(\alpha)}} e^{-\beta E_n^{(\alpha)}} \tag{7}$$

and

$$\hat{H}^{(\alpha)}\big|E_n^{(\alpha)}\big\rangle = E_n^{(\alpha)}\big|E_n^{(\alpha)}\big\rangle, \tag{8}$$

where α labels symmetry sectors of the Hamiltonian, N_{sym} is the number of symmetry sectors, $N_{\mathrm{st}}^{(\alpha)}$ is the number of states in a given symmetry sector α satisfying $N_{\mathrm{st}} = \sum_{\alpha=1}^{N_{\mathrm{sym}}} N_{\mathrm{st}}^{(\alpha)}$, and $\hat{H}^{(\alpha)}$ is the block-diagonalized Hamiltonian, i.e., $\hat{H} = \oplus_{\alpha=1}^{N_{\mathrm{sym}}}\hat{H}^{(\alpha)}$.

We consider the Hamiltonian in Eq. (1) on small clusters under the periodic-boundary conditions. The symmetry sectors are labeled as $(\alpha) = (\mathbf{k}, S^z)$, where $\mathbf{k}$ is the momentum and S^z is the eigenvalue of $\hat{S}^z = \sum_{i=1}^{L}\hat{S}_i^z$, and L is the number of sites. This labeling of the symmetry sectors results in $N_{\mathrm{sym}} = L(L+1)$. Figure 2 shows the available momenta for the $L = 6 \times 6$ cluster, which is the largest size used in the present study. In Appendix A, we describe an algorithm to

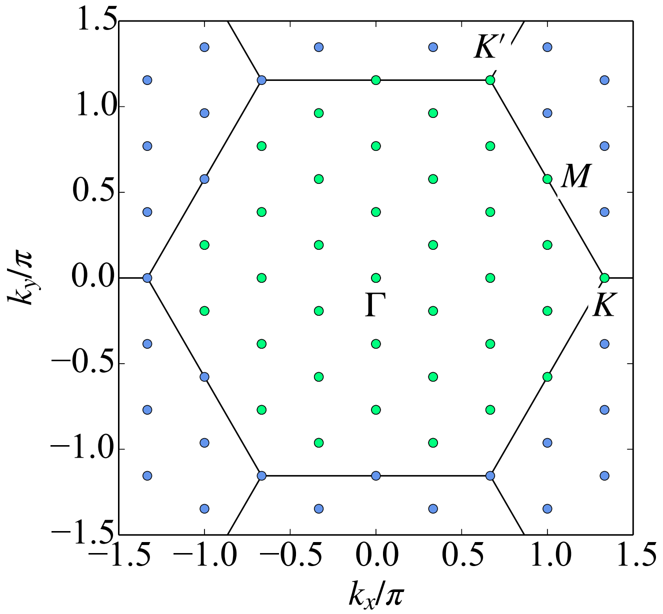

FIG. 2. Available momenta $\mathbf{k} = (k_x, k_y)$ for the $L = 6 \times 6$ cluster under the periodic boundary conditions. Solid lines denote the Brillouin-zone boundaries and light green circles indicate the 36 momenta inside the first Brillouin zone. High symmetric momenta, Γ: (0,0), K: $(4\pi/3, 0)$, M: $(\pi, \pi/\sqrt{3})$, and K': $(2\pi/3, 2\pi/\sqrt{3})$, are also indicated.

find a spin configuration for a given state label in the fixed-magnetization Hilbert space.

We evaluate $Z^{(\alpha)}$ numerically exactly if $N_{\mathrm{st}}^{(\alpha)} \leqslant 10^4$. For evaluation of $Z^{(\alpha)}$ with larger $N_{\mathrm{st}}^{(\alpha)}$, we employ the finite-temperature Lanczos method [70–72] combined with the block-Lanczos algorithm described in the following sections. Below we drop the superscript (α) labeling the symmetry sectors for brevity.

B. Random-phase state

Following Refs. [73,74], here we review some properties of the random-phase states, which is relevant to the stochastic evaluation of the trace. Consider a state $|r\rangle$ such that

$$|r\rangle = \sum_{x=1}^{N_{\mathrm{st}}} \mathrm{e}^{\mathrm{i}\theta_x^r} |x\rangle, \tag{9}$$

where $\{|x\rangle\}$ is an arbitrary complete orthonormal set satisfying $\hat{1} = \sum_{x=1}^{N_{\mathrm{st}}} |x\rangle\langle x|$ and $\langle x|x'\rangle = \delta_{xx'}$, and θ_x^r are random variables distributing uniformly in $[0, 2\pi)$ [75]. Notice that $|r\rangle$ is *not* normalized because $\langle r|r\rangle = N_{\mathrm{st}}$.

We now define a statistical average as

$$\langle\langle \cdots \rangle\rangle = \lim_{R\to\infty} \frac{1}{R} \sum_{r=1}^{R} \cdots, \tag{10}$$

where r denotes a different set of the random variables. Since $\langle\langle \mathrm{e}^{\mathrm{i}\theta_x^r} \rangle\rangle = 0$ and $\langle\langle (\mathrm{e}^{\mathrm{i}\theta_{x'}^r})^* \mathrm{e}^{\mathrm{i}\theta_x^r} \rangle\rangle = \langle\langle \mathrm{e}^{\mathrm{i}(\theta_x^r - \theta_{x'}^r)} \rangle\rangle = \delta_{xx'}$, we can easily show that $|r\rangle$'s are statistically complete

$$\langle\langle |r\rangle\langle r| \rangle\rangle = \sum_{x=1}^{N_{\mathrm{st}}} |x\rangle\langle x| = \hat{1}. \tag{11}$$

The expectation value of operator $\hat{O}$ with respect to $|r\rangle$ is given by

$$\langle r|\hat{O}|r\rangle = \sum_{x=1}^{N_{\mathrm{st}}} \langle x|\hat{O}|x\rangle + \sum_{x=1}^{N_{\mathrm{st}}} \sum_{x'=1}^{N_{\mathrm{st}}} \left(\mathrm{e}^{\mathrm{i}(\theta_x^r - \theta_{x'}^r)} - \delta_{xx'}\right) \langle x'|\hat{O}|x\rangle. \tag{12}$$

Therefore, the trace can be evaluated stochastically as

$$\mathrm{Tr}[\hat{O}] = \sum_{x=1}^{N_{\mathrm{st}}} \langle x|\hat{O}|x\rangle = \langle\langle \langle r|\hat{O}|r\rangle \rangle\rangle. \tag{13}$$

Finally, if the statistical average is truncated at a finite number R of the random-phase states in Eq. (13), the leading error $|\delta O|$, where δO is the second term of the right-hand side of Eq. (12), is estimated as [73,74]

$$\begin{aligned} |\delta O|^2 &= \frac{1}{R} \sum_{x \neq x'} |\langle x'|\hat{O}|x\rangle|^2 \\ &= \frac{1}{R} \left(\mathrm{Tr}[\hat{O}^2] - \sum_{x=1}^{N_{\mathrm{st}}} \langle x|\hat{O}|x\rangle^2 \right). \end{aligned} \tag{14}$$

Here, $\hat{O}$ is assumed to be a Hermitian operator. Note, however, that $\hat{O} = \mathrm{e}^{-\beta\hat{H}}\hat{A}$ is not Hermitian if $\hat{A}$ does not commute with $\hat{H}$, even if $\hat{A}$ itself is Hermitian. In such a case, $\hat{O}$ can still be chosen Hermitian if the symmetric form

$$\hat{O} = \mathrm{e}^{-\beta\hat{H}/2} \hat{A} \mathrm{e}^{-\beta\hat{H}/2} \tag{15}$$

is used as in Eq. (5).

C. Finite-temperature Lanczos method

From Eqs. (10) and (13) we obtain

$$Z = \lim_{R\to\infty} \frac{1}{R} \sum_{r=1}^{R} \langle r|\mathrm{e}^{-\beta\hat{H}}|r\rangle. \tag{16}$$

Now the matrix element $\langle r|\mathrm{e}^{-\beta\hat{H}}|r\rangle$ has to be evaluated. If the full diagonalization of $\hat{H}$ were possible, the matrix element could be evaluated exactly by inserting the identity with the eigenstates $\hat{P}_{\mathrm{Eig}} = \sum_{n=1}^{N_{\mathrm{st}}} |E_n\rangle\langle E_n| = \hat{1}$. In the finite-temperature Lanczos method, $\hat{P}_{\mathrm{Eig}}$ is approximated by the projection onto the Ritz states $\hat{P}_{\mathrm{Ritz}} = \sum_{l=1}^{N_{\mathrm{L}}} |\epsilon_l^r\rangle\langle\epsilon_l^r|$, where $|\epsilon_l^r\rangle$ is the lth Ritz state associated with the Ritz value ϵ_l^r obtained by the Lanczos algorithm terminated at the N_{L}th step of the Lanczos iteration started with the initial state $|r\rangle$. The partition function is thus approximated as

$$Z \approx \frac{1}{R} \sum_{r=1}^{R} \langle r|\mathrm{e}^{-\beta\hat{H}}|r\rangle \approx \frac{1}{R} \sum_{r=1}^{R} \sum_{l=1}^{N_{\mathrm{L}}} \mathrm{e}^{-\beta\epsilon_l^r} \left|\langle\epsilon_l^r|r\rangle\right|^2, \tag{17}$$

where the first approximation is made by truncating the number of the random states at a finite value R, and the second approximation is made by approximating the Boltzmann factor as $\mathrm{e}^{-\beta\hat{H}} \approx \mathrm{e}^{-\beta\hat{H}} \hat{P}_{\mathrm{Ritz}} = \sum_{l=1}^{N_{\mathrm{L}}} \mathrm{e}^{-\beta\epsilon_l^r} |\epsilon_l^r\rangle\langle\epsilon_l^r|$. Equation

(17) is the approximate partition function calculated in the finite-temperature Lanczos method [70–72]. Notice that since $|r\rangle$ defined in Eq. (9) is not normalized, differently from Refs. [70–72], the factor N_{st} does not appear in Eq. (17). Such a factor is taken into account in $|\langle\epsilon_l^r|r\rangle|^2$ in our formulation.

D. Block Lanczos algorithm

Here, we describe the block Lanczos algorithm [76–79] to adopt it for the finite-temperature Lanczos method. As the initial states, we first generate M_{B} random-phase states

$$|r_1\rangle,\ |r_2\rangle,\quad \cdots,\quad |r_{M_{\mathrm{B}}}\rangle. \tag{18}$$

To describe the algorithm, it is convenient to move to the matrix notation. Let $\boldsymbol{Y} \in \mathbb{C}^{N_{\mathrm{st}}\times M_{\mathrm{B}}}$ be a matrix representation of the set of random-phase states in Eq. (18) in the orthonormal basis $\{|x\rangle\}$ used in Eq. (9), i.e.,

$$[\boldsymbol{Y}]_{xb} = \langle x|r_b\rangle = \mathrm{e}^{\mathrm{i}\theta_x^{r_b}}. \tag{19}$$

Namely, $\boldsymbol{Y}$ contains M_{B} random-phase vectors as column vectors.

Since the M_{B} random-phase vectors are not orthonormalized to each other, $\boldsymbol{Y}$ itself cannot be used as the initial vectors for the block Lanczos algorithm. Instead, M_{B} orthonormalized vectors can be obtained from a QR factorization of $\boldsymbol{Y}$ as

$$\boldsymbol{Y} = \boldsymbol{Q}_1\boldsymbol{B}_0, \tag{20}$$

where $\boldsymbol{Q}_1 \in \mathbb{C}^{N_{\mathrm{st}}\times M_{\mathrm{B}}}$ satisfies $\boldsymbol{Q}_1^\dagger\boldsymbol{Q}_1 = \boldsymbol{I}$ and $\boldsymbol{B}_0 \in \mathbb{C}^{M_{\mathrm{B}}\times M_{\mathrm{B}}}$ is an upper triangular matrix satisfying $\boldsymbol{Y}^\dagger\boldsymbol{Y} = \boldsymbol{B}_0^\dagger\boldsymbol{B}_0$. Now $\boldsymbol{Q}_1$ can be used as the initial vectors for the block-Lanczos algorithm. Block-Lanczos vectors $\boldsymbol{Q}_2, \boldsymbol{Q}_3, \cdots, \boldsymbol{Q}_{k_{\max}}$ with $k_{\max} = N_{\mathrm{L}}/M_{\mathrm{B}}$ are constructed successively by iterating the following procedures for $k = 1$ to $k_{\max}$:

$$\boldsymbol{A}_k := \boldsymbol{Q}_k^\dagger\boldsymbol{H}\boldsymbol{Q}_k \tag{21}$$

$$\boldsymbol{X}_k := \boldsymbol{H}\boldsymbol{Q}_k - \boldsymbol{Q}_k\boldsymbol{A}_k - \boldsymbol{Q}_{k-1}\boldsymbol{B}_{k-1}^\dagger \tag{22}$$

$$\boldsymbol{X}_k =: \boldsymbol{Q}_{k+1}\boldsymbol{B}_k, \tag{23}$$

where $\boldsymbol{Q}_0 := \boldsymbol{0}$ and $[\boldsymbol{H}]_{xx'} = \langle x|\hat{H}|x'\rangle$ is the matrix representation of $\hat{H}$. The procedure in Eq. (23) should be read as the QR factorization of $\boldsymbol{X}_k \in \mathbb{C}^{N_{\mathrm{st}}\times M_{\mathrm{B}}}$ yielding the $(k+1)$st block-Lanczos vectors $\boldsymbol{Q}_{k+1} \in \mathbb{C}^{N_{\mathrm{st}}\times M_{\mathrm{B}}}$ with $\boldsymbol{Q}_{k'}^\dagger\boldsymbol{Q}_k = \delta_{k',k}\boldsymbol{I}$ and an upper-triangular matrix $\boldsymbol{B}_k \in \mathbb{C}^{M_{\mathrm{B}}\times M_{\mathrm{B}}}$. The procedure in Eq. (21) requires M_{B} matrix-vector multiplications. Note that N_{L} is assumed to be a multiple of M_{B} for simplicity. However, if N_{L} is not a multiple of M_{B}, $k_{\max}$ should be read as $\mathrm{nint}(N_{\mathrm{L}}/M_{\mathrm{B}})$ for example and N_{L} below as $k_{\max}M_{\mathrm{B}}$, where $\mathrm{nint}(\cdot)$ denotes the nearest-integer function.

Defining $\tilde{\boldsymbol{Q}}_k = (\boldsymbol{Q}_1, \cdots, \boldsymbol{Q}_k) \in \mathbb{C}^{N_{\mathrm{st}}\times kM_{\mathrm{B}}}$, $\boldsymbol{T}_k = \tilde{\boldsymbol{Q}}_k^\dagger\boldsymbol{H}\tilde{\boldsymbol{Q}}_k \in \mathbb{C}^{kM_{\mathrm{B}}\times kM_{\mathrm{B}}}$ can be constructed after the procedure (21) of the kth block-Lanczos iteration. It follows from Eqs. (21)–(23) that $\boldsymbol{Q}_{j'}^\dagger\boldsymbol{H}\boldsymbol{Q}_j = \boldsymbol{A}_j\delta_{j',j} + \boldsymbol{B}_j\delta_{j',j+1} + \boldsymbol{B}_{j'}^\dagger\delta_{j',j-1}$. Therefore, $\boldsymbol{T}_k$ is a Hermitian-band matrix of the form

$$\boldsymbol{T}_k = \begin{bmatrix} \boldsymbol{A}_1 & \boldsymbol{B}_1^\dagger & 0 & \cdots & 0 \\ \boldsymbol{B}_1 & \boldsymbol{A}_2 & \boldsymbol{B}_2^\dagger & \ddots & \vdots \\ 0 & \ddots & \ddots & \ddots & 0 \\ \vdots & \ddots & \boldsymbol{B}_{k-2} & \boldsymbol{A}_{k-1} & \boldsymbol{B}_{k-1}^\dagger \\ 0 & \cdots & 0 & \boldsymbol{B}_{k-1} & \boldsymbol{A}_k \end{bmatrix}. \tag{24}$$

A diagonalization of $\boldsymbol{T}_{k_{\max}}$ gives N_{L} Ritz values as its eigenvalues, i.e.,

$$\boldsymbol{D} = \boldsymbol{U}^\dagger\boldsymbol{T}_{k_{\max}}\boldsymbol{U} = \mathrm{diag}\big(\epsilon_1^{\{r\}}, \cdots, \epsilon_{N_{\mathrm{L}}}^{\{r\}}\big), \tag{25}$$

where $\boldsymbol{U}$ is a unitary matrix. Here, the superscript $\{r\}$ denotes that the Ritz values are obtained by the block-Lanczos method with the initial states $\{r\} = \{r_1, r_2, \cdots, r_{M_{\mathrm{B}}}\}$. It follows from Eq. (25) and $\boldsymbol{T}_{k_{\max}} = \tilde{\boldsymbol{Q}}_{k_{\max}}^\dagger\boldsymbol{H}\tilde{\boldsymbol{Q}}_{k_{\max}}$ that $\boldsymbol{D} = (\tilde{\boldsymbol{Q}}_{k_{\max}}\boldsymbol{U})^\dagger\boldsymbol{H}(\tilde{\boldsymbol{Q}}_{k_{\max}}\boldsymbol{U})$. Therefore, the Ritz state $|\epsilon_l^{\{r\}}\rangle$ which satisfies $\hat{H}|\epsilon_l^{\{r\}}\rangle = \epsilon_l^{\{r\}}|\epsilon_l^{\{r\}}\rangle$ and $\langle\epsilon_l^{\{r\}}|\epsilon_{l'}^{\{r\}}\rangle = \delta_{ll'}$ is given by

$$\big\langle x\big|\epsilon_l^{\{r\}}\big\rangle = [\tilde{\boldsymbol{Q}}_{k_{\max}}\boldsymbol{U}]_{xl}. \tag{26}$$

Finally, the overlap between the initial state and the lth Ritz state is given by

$$\begin{aligned} \big\langle\epsilon_l^{\{r\}}\big|r_b\big\rangle &= \big[\boldsymbol{U}^\dagger\tilde{\boldsymbol{Q}}_{k_{\max}}^\dagger\boldsymbol{Y}\big]_{lb} = \big[\boldsymbol{U}^\dagger\tilde{\boldsymbol{Q}}_{k_{\max}}^\dagger\boldsymbol{Q}_1\boldsymbol{B}_0\big]_{lb} \\ &= \sum_{m=1}^{M_{\mathrm{B}}}[\boldsymbol{U}^\dagger]_{lm}[\boldsymbol{B}_0]_{mb}, \end{aligned} \tag{27}$$

where $\boldsymbol{Q}_{j'}^\dagger\boldsymbol{Q}_j = \delta_{j',j}\boldsymbol{I}$ is used in the last equality.

E. Block-extended finite-temperature Lanczos method

Now the block-extended version of the finite-temperature Lanczos method can be formulated. For simplicity, we assume that the number R of the random-phase states is a multiple of the number M_{B} of the block size. Introducing

$$R_{\mathrm{B}} = \frac{R}{M_{\mathrm{B}}}, \tag{28}$$

the approximate partition function in Eq. (17) can be expressed as

$$\begin{aligned} Z &\approx \frac{1}{R}\sum_{r=1}^{R}\langle r|\mathrm{e}^{-\beta\hat{H}}|r\rangle = \frac{1}{R_{\mathrm{B}}M_{\mathrm{B}}}\sum_{r=1}^{R_{\mathrm{B}}}\sum_{b=1}^{M_{\mathrm{B}}}\langle r_b|\mathrm{e}^{-\beta\hat{H}}|r_b\rangle \\ &\approx \frac{1}{R_{\mathrm{B}}}\sum_{r=1}^{R_{\mathrm{B}}}\sum_{l=1}^{N_{\mathrm{L}}}\mathrm{e}^{-\beta\epsilon_l^{\{r\}}}\left(\frac{1}{M_{\mathrm{B}}}\sum_{b=1}^{M_{\mathrm{B}}}\big|\big\langle\epsilon_l^{\{r\}}\big|r_b\big\rangle\big|^2\right). \end{aligned} \tag{29}$$

On the equality of the first line, the $R\,(=R_{\mathrm{B}}M_{\mathrm{B}})$ random-phase states are simply relabeled by a combination of the subscripts r and b. To obtain the second line, the projection operator $\hat{P}_{\mathrm{Ritz}} = \sum_{l=1}^{N_{\mathrm{L}}}|\epsilon_l^{\{r\}}\rangle\langle\epsilon_l^{\{r\}}|$ is inserted. A formal difference from the standard finite-temperature Lanczos method is that the overlap squared, $|\langle\epsilon_l^r|r\rangle|^2$, in Eq. (17) is replaced by the averaged one over the M_{B} random-phase states, $\sum_{b=1}^{M_{\mathrm{B}}}|\langle\epsilon_l^{\{r\}}|r_b\rangle|^2/M_{\mathrm{B}}$, in Eq. (29). Here, the overlap $\langle\epsilon_l^{\{r\}}|r_b\rangle$ can be calculated through Eq. (27). Obviously, Eq. (29) reproduces Eq. (17) when $M_{\mathrm{B}} = 1$.

Similarly to the partition function, the numerator of Eq. (5) is approximated as

$$\mathrm{Tr}[\mathrm{e}^{-\beta\hat{H}/2}\hat{A}\mathrm{e}^{-\beta\hat{H}/2}] \approx \frac{1}{R}\sum_{r=1}^{R}\langle r|\mathrm{e}^{-\beta\hat{H}/2}\hat{A}\mathrm{e}^{-\beta\hat{H}/2}|r\rangle$$
$$\approx \frac{1}{R_{\mathrm{B}}}\sum_{r=1}^{R_{\mathrm{B}}}\sum_{l=1}^{N_{\mathrm{L}}}\sum_{l'=1}^{N_{\mathrm{L}}}\mathrm{e}^{-\beta(\epsilon_l^{\{r\}}+\epsilon_{l'}^{\{r\}})/2}$$
$$\times\left(\frac{1}{M_{\mathrm{B}}}\sum_{b=1}^{M_{\mathrm{B}}}\langle r_b|\epsilon_{l'}^{\{r\}}\rangle\langle\epsilon_{l'}^{\{r\}}|\hat{A}|\epsilon_l^{\{r\}}\rangle\langle\epsilon_l^{\{r\}}|r_b\rangle\right). \qquad (30)$$

Here, the right-most expression of Eq. (5) is adopted as in the low-temperature Lanczos method [80]. If $\hat{A}$ commutes with $\hat{H}$, then $|\epsilon_l^{\{r\}}\rangle$ are simultaneous eigenstates of $\hat{A}$ and $\hat{H}$. In this case, Eq. (30) can be further simplified because $\langle\epsilon_{l'}^{\{r\}}|\hat{A}|\epsilon_l^{\{r\}}\rangle = A_l^{\{r\}}\delta_{ll'}$, where $A_l^{\{r\}}$ is an eigenvalue of $\hat{A}$.

A nice property of the block-extended version of the finite-temperature Lanczos method [Eqs. (29) and (30)] is that one can flexibly choose R_{B} and M_{B} to exploit the computational resource efficiently. For example, the summation $\sum_{r=1}^{R_{\mathrm{B}}}\cdots$ can be done independently for each r, while a block size of $M_{\mathrm{B}} > 1$ allows for the better performance in a single process as compared to the case of $M_{\mathrm{B}} = 1$. To be more specific, let us consider an on-the-fly Hamiltonian multiplication to the block-Lanczos vectors. In that case, the dominant computational costs are generating Hamiltonian matrix elements rather than performing simple multiply-add operations. Since the block Lanczos method multiplies the Hamiltonian matrix to M_{B} vectors simultaneously, M_{B} times less operations for generating the matrix elements are required to achieve the same number of Hamiltonian-vector multiplications, as compared to the standard Lanczos method. We remark that such simultaneous Hamiltonian multiplication to vectors can be employed also in the polynomial expansion technique [74].

In the block Lanczos method, at least $2M_{\mathrm{B}}$ vectors (of N_{st} dimension) have to be stored. When the required memory for storing the $2M_{\mathrm{B}}$ vectors exceeds the limit of the available resource, one can simply reduce the number M_{B} of the block size, or even switch to the standard finite-temperature Lanczos method merely by setting $M_{\mathrm{B}} = 1$. Fortunately, the smaller number R of samplings is required for the larger N_{st} to maintain a statistical accuracy (see for example Refs. [81,82] and Sec. II F).

Now we have three parameters R_{B}, M_{B}, and N_{L} for controlling the accuracy of the block-extended version of the finite-temperature Lanczos method. Values of these parameters will be specified for each result in Sec. III.

F. Connection with the canonical thermal-pure-quantum state

The finite-temperature Lanczos method for observables commuting with $\hat{H}$ [70–72], the low-temperature Lanczos method for observables not commuting with $\hat{H}$ [80], and the block-extended version of the finite-temperature Lanczos method for observables not commuting with $\hat{H}$ described in the previous section, can all be regarded as a method that makes use of the canonical thermal-pure-quantum (CTPQ) state [83], as recently demonstrated with the standard finite-temperature Lanczos method in Ref. [84]. For example, the matrix element $\langle r_b|\mathrm{e}^{-\beta\hat{H}}|r_b\rangle$ appearing in Eq. (29) is the inner product of the (unnormalized) CTPQ state $\mathrm{e}^{-\beta\hat{H}/2}|r_b\rangle$. There are several ways to evaluate matrix functions operated to vectors without full diagonalization, such as polynomial expansion techniques [85–93]. With the Lanczos method used here, the CTPQ state is approximated by a linear combination of the N_{L} Ritz states $|\epsilon_l^{\{r\}}\rangle$ as

$$\mathrm{e}^{-\beta\hat{H}/2}|r_b\rangle \approx \hat{P}_{\mathrm{Ritz}}\mathrm{e}^{-\beta\hat{H}/2}|r_b\rangle = \sum_{l=1}^{N_{\mathrm{L}}}\mathrm{e}^{-\beta\epsilon_l^{\{r\}}/2}\langle\epsilon_l^{\{r\}}|r_b\rangle|\epsilon_l^{\{r\}}\rangle. \qquad (31)$$

In this sense, although it is difficult to estimate the systematic error associated with the approximation made in Eq. (31), one can still refer to the convergence analysis of CTPQ states [83]. For instance, the better convergence in probability to the ensemble average is expected for the larger $\mathcal{D}(T) = \mathrm{e}^{Ls(T)}$ with $s(T)$ being the entropy density. Here $\mathcal{D}(T)$ can be interpreted as a temperature-dependent effective dimension of the Hilbert space, because it satisfies $\lim_{T\to\infty}\mathcal{D}(T) = N_{\mathrm{st}}$ and $\lim_{T\to 0}\mathcal{D}(T) = g$, where g is the ground-state degeneracy.

Note that the (block) Lanczos method approximates well the extremal eigenvalues and eigenstates within a few hundreds of the Lanczos steps N_{L}, almost independently of the realization of the initial random-phase state $|r_b\rangle$. Therefore, the (block) Lanczos approach to the matrix exponential, as in Eq. (31), complements the CTPQ approach at low temperatures by its fast convergence to the ground state and low-lying excited states for each symmetry sector. In particular, the block Lanczos method can better approximate the low-lying excited states, especially within the block size, as compared to the standard Lanczos method [76]. On the other hand, empirically, the convergence of the (block) Lanczos method to the inner (i.e., nonextremal) eigenpairs with dense spectra seems "random," in the sense that the convergence depends on the realization of $|r_b\rangle$ for fixed N_{L}, as observed in spectra of dynamical correlation functions [72]. This implies that relatively large error bars are expected at temperatures where the specific heat exhibits a peak, because the larger specific heat indicates the larger fluctuation of the internal energy $\langle\hat{H}\rangle$, thus implying the denser eigenspectra of $\hat{H}$. Finally, we remark that a connection between the finite-temperature Lanczos method and the eigenstate-thermalization hypothesis [94,95] has been discussed recently in Ref. [96].

III. RESULTS

Figure 3 shows the specific heat

$$c(T) = \frac{1}{LT^2}[\langle\hat{H}^2\rangle - \langle\hat{H}\rangle^2], \qquad (32)$$

the entropy density

$$s(T) = \frac{1}{LT}[\langle\hat{H}\rangle + T\ln Z], \qquad (33)$$

the uniform magnetic susceptibility

$$\chi(T) = \frac{1}{LT}[\langle(\hat{S}^z)^2\rangle - \langle\hat{S}^z\rangle^2], \qquad (34)$$

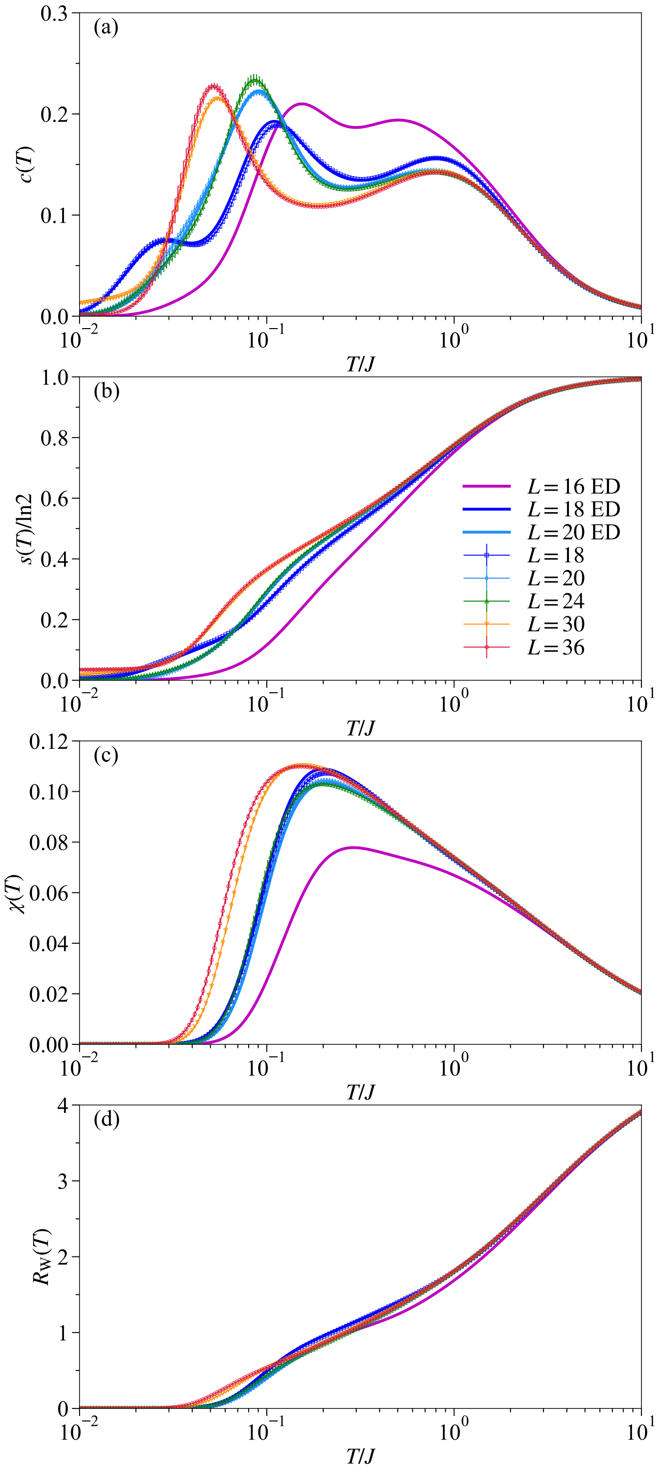

FIG. 3. (a) Specific heat $c(T)$, (b) entropy density $s(T)$, (c) uniform susceptibility $\chi(T)$, and (d) Wilson ratio $R_{\rm W}(T)$ at $J_{\rm c}/J = 0.07$ for $L = 4\times 4$, 18, 5×4, 6×4, 30, and 6×6 clusters (see Fig. 4). Solid lines are results obtained by the full exact diagonalization. Block-Lanczos parameters are $R_{\rm B} = 24$, $M_{\rm B} = 6$, and $N_{\rm L} = 120$ for $L = 4\times 5$, $R_{\rm B} = 24$, $M_{\rm B} = 8$, and $N_{\rm L} = 160$ for $L = 18$, $R_{\rm B} = 8$, $M_{\rm B} = 8$, and $N_{\rm L} = 200$ for $L = 6\times 4$, $R_{\rm B} = 6$, $M_{\rm B} = 8$, and $N_{\rm L} = 320$ for $L = 30$, and $R_{\rm B} = 6$, $M_{\rm B} = 4$ for $0 \leqslant |S_z| \leqslant 1$, $M_{\rm B} = 6$ for $2 \leqslant |S_z| \leqslant 5$, $M_{\rm B} = 6$ for $6 \leqslant |S_z|$, and $N_{\rm L} = 720$ for $L = 6\times 6$.

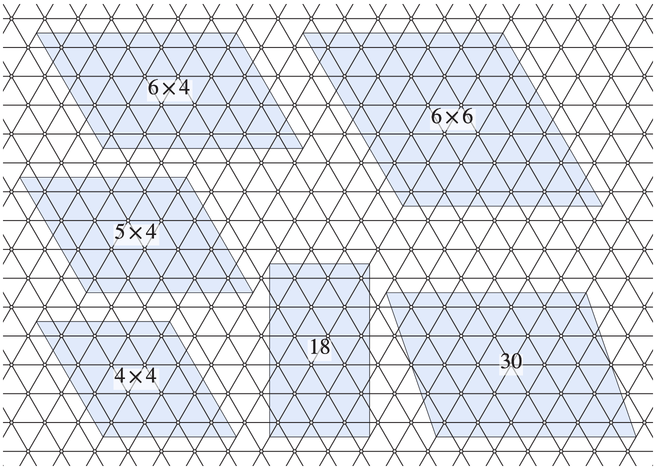

FIG. 4. Cluster structures used for the calculations. The periodic boundary conditions are imposed.

and the generalized temperature-dependent Wilson ratio [97]

$$R_{\rm W}(T) = \frac{4\pi^2 T\chi(T)}{3s(T)} \tag{35}$$

at $J_{\rm c}/J = 0.07$ for $L = 4\times 4$, 18, 5×4, 6×4, 30, and 6×6 (see Fig. 4). Notice that the entropy density $s(T)$ is normalized with respect to $\lim_{T\to\infty} s(T) = \ln 2$ in the figure. Since these quantities involve only the thermal average of the quantities that commute with $\hat{H}$, the calculations are particularly efficient as compared to the quantities that do not commute with $\hat{H}$. Each of the error bars represents the standard error of the mean $\tilde{\sigma}/\sqrt{R_{\rm B}}$ with $\tilde{\sigma}$ being the estimated standard deviation defined by

$$\tilde{\sigma} = \sqrt{\frac{1}{R_{\rm B}-1}\sum_{r=1}^{R_{\rm B}}(X_r - \bar{X})^2}, \tag{36}$$

where X_r is calculated $c(T)$, $s(T)$, $\chi(T)$, or $R_{\rm W}(T)$ but for a given r (without averaging over r), and $\bar{X}$ is $c(T)$, $s(T)$, $\chi(T)$, or $R_{\rm W}(T)$ itself. For comparison, the full-diagonalization results are also shown in Fig. 3 for $L \leqslant 20$. It is confirmed for $L = 18$ and $L = 5\times 4$ that the results obtained by the block-extended version of the finite-temperature Lanczos method mostly coincide with the full-diagonalization results within error bars [98].

Figure 5 shows the $J_{\rm c}$ dependence of $c(T)$, $s(T)$, $\chi(T)$, and $R_{\rm W}(T)$ for $L = 6\times 6$, which is the largest cluster available and preserves all the symmetries of the triangular lattice. Without the ring-exchange interaction ($J_{\rm c} = 0$), $c(T)$ exhibits a peak around $T/J = 0.2$ and a broad shoulder for $T/J \gtrsim 0.5$, while no significant structure can be found in $s(T)$. This is in good agreement with the previous results calculated by the finite-temperature Lanczos and the exponential tensor-renormalization-group methods [68,99–101]. At low temperatures, a power-law dependence of $c(T) \sim T^2$ is expected with the Néel order [102]. However, such a power-law dependence is not found here due to the energy gap intrinsic to the finite-size calculation.

For $J_{\rm c}/J \geqslant 0.04$, the specific heat $c(T)$ shows a double-peak structure with a broad high-temperature peak at $T =$

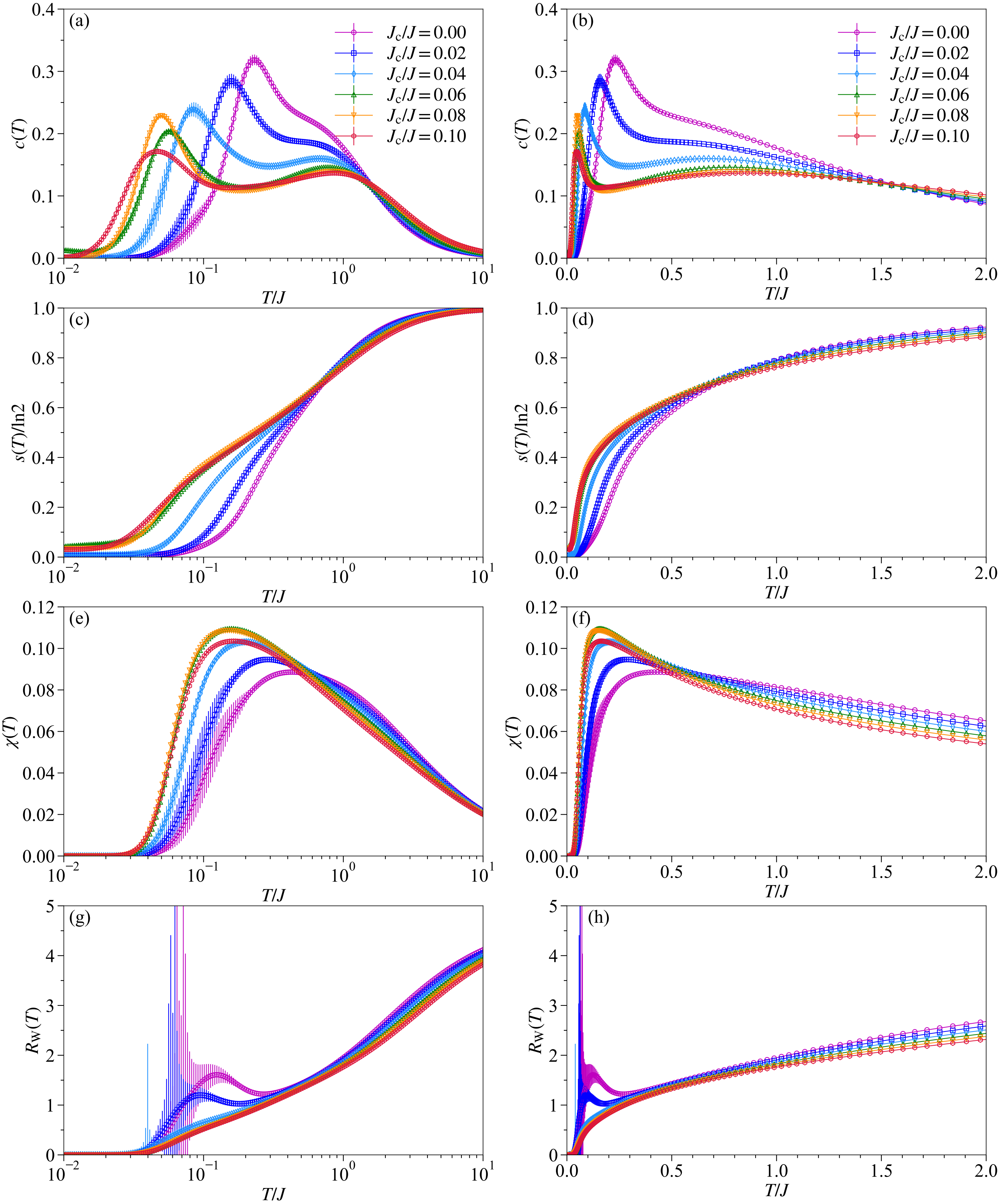

FIG. 5. Semilog (left) and linear (right) plots of (a),(b) specific heat $c(T)$, (c),(d) entropy density $s(T)$, (e),(f) uniform susceptibility $\chi(T)$, and (g),(h) Wilson ratio $R_W(T)$ for several values of J_c/J, indicated in the figures, and $L = 6 \times 6$. Block-Lanczos parameters are $R_B = 6$, $M_B = 4$ for $0 \leqslant |S_z| \leqslant 1$, $M_B = 6$ for $2 \leqslant |S_z| \leqslant 5$, $M_B = 6$ for $6 \leqslant |S_z|$, and $N_L = 720$.

$T_{\text{high}} \sim J$ and a sharp low-temperature peak at $T = T_{\text{low}} \ll J$. Moreover, it is observed that the high-temperature peak shifts towards higher temperature with increasing J_c/J like $T_{\text{high}} \sim J + 5J_c$. Such a behavior of the high-temperature peak can be expected from Eq. (B5), where the effective nearest-neighbor exchange $J + 5J_c$ becomes a dominant energy scale at high temperatures.

As shown in Fig. 3(a), the low-temperature peak position for $J_c/J = 0.07$ tends to be lowered for the larger clusters, while the high-temperature peak is insensitive to the system size. For example, for the $L = 6 \times 6$ cluster, the high-temperature peak appears at $T_{\text{high}}/J \approx 0.8$ and the low-temperature peak is found at $T_{\text{low}}/J \approx 0.05$. At the highest temperature around $T/J \sim 10$, the entropy density reaches $s = \ln 2 \approx 0.693$, indicating that the system is in the paramagnetic state. In the temperature regime where $c(T)$ shows a dip between the two peaks, $s(T)$ exhibits a shoulderlike structure which is visible in the semilog plot shown in Fig. 5(c). Interestingly, about half of the total entropy $s = \frac{1}{2}\ln 2 \approx 0.347$ remains at such a temperature regime. The shoulderlike structure of $s(T)$ becomes more prominent for the larger system size [see Fig. 3(b)].

As shown in Figs. 5(e) and 5(f), the uniform magnetic susceptibility $\chi(T)$ decreases quickly below temperature T_χ at which $\chi(T)$ takes a maximum. The peak position T_χ varies from $T_\chi \approx 0.3J$ for $J_c/J = 0$ to $T_\chi \approx 0.15J$ for $J_c/J = 0.1$. In particular, a rapid decrease of T_χ can be observed for $0 \leqslant J_c/J \leqslant 0.06$. It is also found that for $J_c/J \geqslant 0.04$ there exists a temperature region where the entropy and specific heat are finite while $\chi(T)$ is almost zero. This implies that many nonmagnetic excitations exist below the first magnetic excitation, which is consistent with the strong-coupling expansion of the Hubbard model [103]. Such low-lying nonmagnetic excited states are thus essential for forming the low-temperature peak in the specific heat.

These characteristic low-lying excitations can be better seen in the temperature-dependent Wilson ratio $R_{\text{W}}(T)$ [97] shown in Figs. 5(g) and 5(h). If this quantity tends to zero, it is indicative that the magnetic excitations are inactive while nonmagnetic ones are active. Although the error bars are too large to discuss its behavior for $T/J < 0.1$ and $J_c/J \lesssim 0.02$, the slight upturn of $R(T)$ for $J_c/J = 0$ at $T/J \sim 0.2$ is consistent with the result for the pure-triangular case reported in Ref. [97]. Despite the large error bars, one can still observe a clear change of behavior in $R_{\text{W}}(T)$ for $T/J < 0.4$ between the parameter regions $J_c/J \leqslant 0.02$ and $J_c/J \geqslant 0.04$.

Finally, it is observed in Fig. 5 that the error bars become larger below the temperature at which the specific heat takes the maximum (the low-temperature maximum for $J \geqslant 0.04$). This behavior is expected from the discussion in Sec. II F.

IV. SUMMARY AND DISCUSSION

The thermodynamic properties of an $S = 1/2$ antiferromagnetic Heisenberg model on the triangular lattice with the ring-exchange interaction have been studied by the block-extended version of the finite-temperature Lanczos method. The results for entropy $s(T)$, uniform magnetic susceptibility $\chi(T)$, and Wilson ratio $R_{\text{W}}(T)$ have shown that there exist low-energy nonmagnetic excitations for $J_c/J \geqslant 0.04$. The specific heat $c(T)$ exhibits a characteristic double-peak structure for $J_c/J \geqslant 0.04$, with the low-temperature peak being caused by these nonmagnetic excitations.

As it is apparent from $s(T)$, $\chi(T)$, and $R_{\text{W}}(T)$, there is a great deal of similarity in the low-lying excitations between the ring-exchange model studied here and the $J_1 - J_2$ model on the triangular lattice or the kagome-lattice antiferromagnet [68,97,104,105]. However, the double-peak structure found here in $c(T)$ for $J_c/J \geqslant 0.04$ distinguishes the ring-exchange model from the other models. Indeed, such a double-peak structure has not been observed in the $J_1 - J_2$ model on the triangular lattice for $J_2/J_1 = 0.1$ and 0.2 [99]. Moreover, the separation of these two peaks for the ring-exchange model is found to be more pronounced with increasing the system size. Such a system-size dependence of the low-temperature peak positions is in contrast to that in the kagome-lattice antiferromagnet where the lower-temperature peak moves towards higher temperatures with increasing the system size [81,106]. Instead, a system-size dependence similar to the ring-exchange model found here has also been observed in the Kitaev model [107]. This implies that the excitations corresponding to the high-temperature peak are spatially local, while those corresponding to the low-temperature peak are not.

It is interesting to compare the present results with the recent experiments on $\text{Ba}_2\text{CoNb}_6\text{O}_{24}$, which is considered to be the $S = 1/2$ two-dimensional triangular-lattice Heisenberg antiferromagnet with a nearest-neighbor coupling $J = 0.144$ meV [66] or $J = 1.66 \pm 0.06$ K [67]. In this material, no indication of the magnetic order has been found in the thermodynamic measurements down to $T = 80$ mK. After subtraction of the phonon contribution ($\propto T^3$), the specific heat takes a single-peak structure. Considering the absence of the double-peak structure in the specific heat, the case without the ring-exchange interaction (i.e., $J_c/J = 0$) is rather more relevant to $\text{Ba}_2\text{CoNb}_6\text{O}_{24}$ than the ring-exchange model. In the literature [66,67], the absence of the 120° long-range order at finite temperatures is attributed to a realization of the Mermin-Wagner theorem [108] on the real material.

Thermodynamic properties of $1T$-TaS_2 have also been measured experimentally [109–111]. So far, no indication of a double-peak structure in the magnetic heat capacity has been reported. For example, only a single broad hump in the magnetic heat capacity has been observed in Ref. [109]. However, the entropy at high temperature, obtained by integrating the magnetic heat capacity over the whole temperature region measured, reaches only ≈40% of ln 2 [109]. If we assume that there exists a sharp peak in the magnetic heat capacity at temperature lower than the experimental reach, such a missing entropy is not inconsistent with our results, because our result implies that $s \approx \frac{1}{2}\ln 2$ remains at the temperature where $c(T)$ exhibits a dip. Therefore, a further study on the missing entropy in $1T$-TaS_2 is highly desirable. We should note that a similar scenario on the missing entropy and the double-peak structure in the heat capacity had been discussed in the context of nuclear magnetism of ^{3}He film [112], which was resolved by the lower-temperature measurement of the heat capacity [55].

In Appendix B, we study the effect of the ring-exchange interaction J_c on the spin-wave dispersion in the 120° Néel ordered state, within the linear spin-wave theory. It is found that the spin-excitation energies near the M point and symmetrically equivalent points are decreased drastically with J_c. However, the spin-wave analysis, which takes into account only the magnon excitation, was not able to capture the characteristic thermodynamic features, including the double-peak structure of $c(T)$, found in our numerical calculations. In particular, the microscopic understanding of the double-peak structure in $c(T)$ found here requires a rather systematic analysis for larger clusters and is left for future study.

ACKNOWLEDGMENTS

The authors are grateful to Tao Li for useful discussions and Yusuke Nomura and Shohei Miyakoshi for helpful comments. The numerical computations have been done on HOKUSAI GreatWave and HOKUSAI BigWaterfall supercomputers at RIKEN under Project Nos. G19011 and G20015. This work was supported by Grant-in-Aid for Research Activity start-up (No. 19K23433) and Grant-in-Aid for Scientific Research (B) (No. 18H01183) from MEXT, Japan.

APPENDIX A: ALGORITHM TO FIND A SPIN CONFIGURATION FOR A GIVEN STATE LABEL IN A FIXED-MAGNETIZATION HILBERT SPACE

The two-dimensional search technique introduced by Lin [113] is an efficient method to find a state label j for a given spin configuration i, i.e., $j(i)$, with a relatively small amount of storage, whose dimension is $2 \times 2^{L/2}$. Here, a set of the binary digits $\{b_l\}$ that represents i with

$$i = \sum_{l=1}^{L} b_l 2^{l-1} \equiv (b_L b_{L-1} \dots b_1)_2 \tag{A1}$$

is assigned to a spin configuration, by identifying $b_l = 0$ ($b_l = 1$) with the presence of a spin-↓ (spin-↑) at the lth site.

The inverse table, which returns a spin configuration i for a given state label j, i.e., $i(j)$, is often stored. For a fixed-magnetization Hilbert space, the length of the inverse table is given by the binomial coefficient

$$\binom{L}{N_\uparrow} = \frac{L!}{N_\uparrow!(L - N_\uparrow)!} = \binom{L}{L - N_\uparrow}, \tag{A2}$$

where N_σ is the number of spins with spin σ, $N_\uparrow + N_\downarrow = L$, and the magnetization is given by $S^z = (N_\uparrow - N_\downarrow)/2$. The range of the state label j can be chosen as

$$1 \leqslant j \leqslant \binom{L}{N_\uparrow}. \tag{A3}$$

For a concrete example of the correspondence between j and i, see Table I. Since the range of i is given by

$$2^{N_\uparrow} - 1 \leqslant i \leqslant 2^L - 2^{L-N_\uparrow}, \tag{A4}$$

i might be 64 bit integer for $L \geqslant 32$. An algorithm that returns a spin configuration i for a given state label j may be useful when spin configurations i do not appear sequentially during the calculation of matrix elements of the Hamiltonian, due to, for example, a parallelization of the on-the-fly matrix-vector multiplication.

TABLE I. Correspondence between state label j and spin configuration i for $L = 6$ and $N_\uparrow = 3$. Both j and i are assumed to be in ascending order.

j	$i(L, N_\uparrow, j)$	j	$i(L, N_\uparrow, j)$
1	$(000111)_2 = 7$	11	$(100011)_2 = 35$
2	$(001011)_2 = 11$	12	$(100101)_2 = 37$
3	$(001101)_2 = 13$	13	$(100110)_2 = 38$
4	$(001110)_2 = 14$	14	$(101001)_2 = 41$
5	$(010011)_2 = 19$	15	$(101010)_2 = 42$
6	$(010101)_2 = 21$	16	$(101100)_2 = 44$
7	$(010110)_2 = 22$	17	$(110001)_2 = 49$
8	$(011001)_2 = 25$	18	$(110010)_2 = 50$
9	$(011010)_2 = 26$	19	$(110100)_2 = 52$
10	$(011100)_2 = 28$	20	$(111000)_2 = 56$

Here we introduce such a function $i(j)$ by assuming that both i and j are in the ascending order, as in Table I. The basic idea is to assign a state label j to one of the shortest paths from the vertex $\binom{L}{L-N_\uparrow}$ to the topmost vertex $\binom{0}{0}$ on Pascal's triangle (see Fig. 6). Since there are $\binom{L}{L-N_\uparrow}$ different paths, a one-to-one correspondence between the shortest paths and $\{j\}$ should exist.

To find a correspondence between binary numbers and the shortest paths on Pascal's triangle, the following combinato-

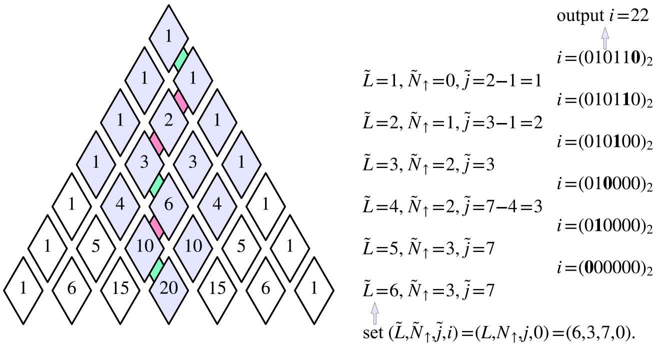

FIG. 6. Schematic figure of the algorithm to find a spin configuration i for a given state label j. The figure should be read from bottom to top to compare with Algorithm 1. For a given set of L, $N_\uparrow$, and j, one of the shortest paths from the vertex $\binom{L}{L-N_\uparrow}$ to the topmost vertex $\binom{0}{0}$ of Pascal's triangle is assigned, and the path determines the spin configuration $i = \sum_{\tilde{L}=1}^{L} b_{\tilde{L}} 2^{\tilde{L}-1} = (b_L b_{L-1} \dots b_1)_2$. The path goes rightward if $\tilde{j} > \binom{\tilde{L}-1}{\tilde{N}_\uparrow}$ (indicated by magenta) or else leftward (indicated by green). The rightward (leftward) path from $\tilde{L}$th row to $\tilde{L} - 1$th row implies that $b_{\tilde{L}} = 1$ ($b_{\tilde{L}} = 0$). The figure refers to the input $(L, N_\uparrow, j) = (6, 3, 7)$, which results in the output $i = (010110)_2 = 22$. The $(N_\uparrow + 1) \times (N_\downarrow + 1) = 16$ vertices on the possible $\binom{6}{3} = 20$ shortest paths are highlighted with shaded blue color, and $b_{\tilde{L}}$ in i is highlighted with boldface. Although a quick return is possible at $\tilde{L} = 3$ in this example, according to the lines 9–11 of Algorithm 1, the remaining processes corresponding to the lines 12–15 of Algorithm 1 for $\tilde{L} \leqslant 3$ are also shown here in this figure.

Algorithm 1 A function that returns a spin configuration i for given number L of sites, number $N_\uparrow$ of up spins, and state label j. Comments are given in the right-most side.

```
Require:
    Input: integer $L$, $N_\uparrow$, and $j$
    $0 \leqslant N_\uparrow \leqslant L$
    $1 \leqslant j \leqslant \binom{L}{N_\uparrow}$
    Temporal integer variables $\tilde{L}$, $\tilde{N}_\uparrow$, and $\tilde{j}$
Ensure:
    Output: integer $i$
    $2^{N_\uparrow} - 1 \leqslant i \leqslant 2^L - 2^{L-N_\uparrow}$
1:  function FIND-CONFIGURATION($L$, $N_\uparrow$, $j$)
2:      $i = 0$                                              ▷ initialization
3:      $\tilde{j} = j$                                      ▷ initialization
4:      $\tilde{N}_\uparrow = N_\uparrow$                    ▷ initialization
5:      for $\tilde{L} = L,\ L-1,\ \ldots,\ 1$ do            ▷ sweep all binary digits of $i$
6:        if $\tilde{j} = 1$ then
7:          $i = i + 2^{\tilde{N}_\uparrow} - 1$             ▷ Eq. (A7)
8:          return $i$                                       ▷ $i$ is determined
9:        else if $\tilde{j} = \binom{\tilde{L}}{\tilde{N}_\uparrow}$ then
10:         $i = i + 2^{\tilde{L}} - 2^{\tilde{L}-\tilde{N}_\uparrow}$   ▷ Eq. (A8)
11:         return $i$                                       ▷ $i$ is determined
12:       else if $\tilde{j} > \binom{\tilde{L}-1}{\tilde{N}_\uparrow}$ then
13:         $i = i + 2^{\tilde{L}-1}$                        ▷ $\tilde{L}$th binary digit of $i$ is 1
14:         $\tilde{j} = \tilde{j} - \binom{\tilde{L}-1}{\tilde{N}_\uparrow}$   ▷ to satisfy Eq. (A9)
15:         $\tilde{N}_\uparrow = \tilde{N}_\uparrow - 1$    ▷ decrement "# of ↑ spins" by 1
16:       end if
17:     end for
18: end fuction
```

rial recursion formula should be reminded;

$$\binom{L}{L-N_\uparrow} = \binom{L-1}{L-N_\uparrow-1} + \binom{L-1}{L-N_\uparrow}. \tag{A5}$$

In terms of Pascal's triangle, Eq. (A5) relates the current vertex (left-hand side) with its upper left vertex (first term of the right-hand side) and upper right vertex (second term of the right-hand side). More specifically, among the total $\binom{L}{L-N_\uparrow}$ spin configurations, $\binom{L-1}{L-N_\uparrow-1} = \binom{L-1}{N_\uparrow}$ spin configurations have "0" at the Lth binary digit, and $\binom{L-1}{L-N_\uparrow} = \binom{L-1}{N_\uparrow-1}$ spin configurations have "1" at the Lth binary digit, assuming that the number of 1's is $N_\uparrow$. By taking into account also the assumption that both i and j are in the ascending order with Eq. (A3), the Lth binary digit b_L of i for a given j is determined as

$$b_L = \begin{cases} 0 & \text{if } j \leqslant \binom{L-1}{N_\uparrow}, \\ 1 & \text{otherwise}. \end{cases} \tag{A6}$$

This property holds for any $(L, N_\uparrow, j)$, implying that i can be determined by repeatedly evaluating the above for the remaining binary digits $\{b_l\}_{l=1}^{L-1}$ with a proper manipulation (decrement) of $(L, N_\uparrow, j)$. A proposed function of finding a spin configuration i for a given set of $(L, N_\uparrow, j)$ is summarized in Algorithm1.

Several remarks on Algorithm 1 are in order.

(1) Binomial coefficients should be calculated and stored in advance for better performance.

(2) Regarding the lines 3–5 of Algorithm 1, the temporal variables $\tilde{j}$, $\tilde{N}_\uparrow$, and $\tilde{L}$ can be considered as temporal state label, temporal number of ↑ spins, and temporal system size, respectively. In terms of the shortest paths on Pascal's triangle, the decrementing loop of $\tilde{L}$ means that the shortest path is determined by climbing up Pascal's triangle from its Lth row, and $\tilde{N}_\uparrow$ is the remaining number of rightward paths. $\tilde{N}_\uparrow$ and $\tilde{j}$ also have to be decremented properly in the loop (lines 14–15 of Algorithm 1), as it will be described in remark (5) below.

(3) Regarding the lines 6–8 of Algorithm 1, the condition $\tilde{j} = 1$ indicates that, among the remaining $\tilde{L}$ binary digits of i, the lowest $\tilde{N}_\uparrow$ digits should be filled with 1's, i.e.,

$$i = (b_L b_{L-1} \ldots b_{\tilde{L}+1} \overbrace{\underbrace{00\ldots0}_{\tilde{L}-\tilde{N}_\uparrow} \underbrace{11\ldots1}_{\tilde{N}_\uparrow}}^{\tilde{L}})_2. \tag{A7}$$

In terms of the shortest paths on Pascal's triangle, this implies that the rest of the path goes first in the upper left direction $\tilde{L} - \tilde{N}_\uparrow$ times and then in the upper right direction $\tilde{N}_\uparrow$ times.

(4) Regarding the lines 9–11 of Algorithm 1, the condition $\tilde{j} = \binom{\tilde{L}}{\tilde{N}_\uparrow}$ indicates that, among the remaining $\tilde{L}$ binary digits

of i, the highest $\tilde{N}_\uparrow$ digits should be filled with 1's, i.e.,

$$i = (b_L b_{L-1} \dots b_{\tilde{L}+1} \overbrace{\underbrace{11\dots1}_{\tilde{N}_\uparrow}\ \underbrace{00\dots0}_{\tilde{L}-\tilde{N}_\uparrow}}^{\tilde{L}})_2. \tag{A8}$$

In terms of the shortest paths on Pascal's triangle, this implies that the rest of the path goes first in the upper right direction $\tilde{N}_\uparrow$ times and then in the upper left direction $\tilde{L} - \tilde{N}_\uparrow$ times.

(5) Regarding the lines 12–15 of Algorithm 1, the condition $\tilde{j} > \binom{\tilde{L}-1}{\tilde{N}_\uparrow}$ indicates that the $\tilde{L}$th binary digit of i is 1, as discussed around Eqs. (A5) and (A6). In terms of the shortest paths on Pascal's triangle, this implies that the rightward path is chosen to go from the $\tilde{L}$th row to the $(\tilde{L} - 1)$th row. As in line 15, $\tilde{N}_\uparrow$ is decreased by 1 because the remaining rightward paths have to be decreased by 1. As in line 14, $\tilde{j}$ has to be decreased in order to satisfy

$$1 \leqslant \tilde{j} \leqslant \binom{\tilde{L}}{\tilde{N}_\uparrow} \tag{A9}$$

for the next loop. This allows us to make use of the relation between the combinatorial recursion and the binary digits for $(\tilde{L}, \tilde{N}_\uparrow, \tilde{j})$.

(6) Although it is not implemented in Algorithm 1, at some $\tilde{L}$ one can switch to refer to a "small" table $i(\tilde{L}, \tilde{N}_\uparrow, \tilde{j})$ stored in advance in the memory to determine the remaining $\tilde{L}$ binary digits of i, instead of fully performing the loop over $\tilde{L}$. One can also implement a quick return when $\tilde{N}_\uparrow = 1$ (when the current vertex is on the line next to the right edge) or $\tilde{L} - \tilde{N}_\uparrow = 1$ (when the current vertex is on the line next to the left edge) is satisfied.

Figure 6 shows a concrete example of the algorithm for $L = 6$, $N_\uparrow = 3$, and $j = 7$. The path from the vertex $\binom{6}{3} = 20$ to the topmost vertex is uniquely determined, and accordingly the algorithm returns the corresponding spin configuration $i(L = 6, N_\uparrow = 3, j = 7) = (010110)_2 = 22$.

The algorithm is applicable also to other models such as the Hubbard model where the total electron configuration can be given as a tensor product of up-spin and down-spin electron configurations, and the t-J model where the total electron configuration can be given as a tensor product of hole and spin configurations, if the Hilbert space is constructed for fixed magnetization and number of electrons.

APPENDIX B: LINEAR SPIN-WAVE THEORY

Here we study the effect of the cyclic exchange interaction J_c on the spin-wave dispersion in the 120° Néel ordered state within the linear spin-wave theory. A comparison of the spin-wave dispersion of the Heisenberg model on the triangular lattice with the nearest and the next-nearest-neighbor interactions (J-J' model) is also made.

1. Full Hamiltonian

Before starting the linear spin-wave approximation, it is convenient to rewrite the full Hamiltonian $\hat{H}$ in terms of the sum of inner products of spin operators. The four-spin exchange term can be written as

$$\hat{P}_{ijkl} + \hat{P}^\dagger_{ijkl} = \frac{1}{4} + \sum_{i'<j'\in\langle ijkl\rangle} \hat{\mathbf{S}}_{i'} \cdot \hat{\mathbf{S}}_{j'} + 4(\hat{Q}_{ijkl} + \hat{Q}_{iljk} - \hat{Q}_{ikjl}), \tag{B1}$$

where

$$\hat{Q}_{ijkl} = (\hat{\mathbf{S}}_i \cdot \hat{\mathbf{S}}_j)(\hat{\mathbf{S}}_k \cdot \hat{\mathbf{S}}_l). \tag{B2}$$

If the sum over all plaquettes $\sum_{\langle ijkl\rangle}$ is performed, the first term (multiplied by J_c) results in

$$J_c \sum_{\langle ijkl\rangle} \frac{1}{4} = \frac{3J_c}{4} L, \tag{B3}$$

because there exist $3L$ plaquettes for the L-site system under periodic-boundary conditions (see Fig. 1). Similarly, the second term results in

$$J_c \sum_{\langle ijkl\rangle} \sum_{i'<j'\in\langle ijkl\rangle} \hat{\mathbf{S}}_{i'} \cdot \hat{\mathbf{S}}_{j'} = 5J_c \sum_{\langle ij\rangle} \hat{\mathbf{S}}_i \cdot \hat{\mathbf{S}}_j + J_c \sum_{\langle\langle ij\rangle\rangle} \hat{\mathbf{S}}_i \cdot \hat{\mathbf{S}}_j, \tag{B4}$$

where $\langle\langle ij\rangle\rangle$ denotes a pair of spins on the next-nearest-neighbor sites i and j on the triangular lattice. The factor 5 in the first term is because the nearest-neighbor bonds $((i', j') = \{(i, j), (j, k), (k, l), (l, i), (j, l)\})$ appear five times in the sum over the plaquettes for the ring-exchange term. Similarly, the factor 1 in the second term is because the next-nearest-neighbor bond $((i', j') = \{(i, k)\})$ appears once for each plaquette and is distinct for different plaquettes. Now the full Hamiltonian is written as

$$\hat{H} = (J + 5J_c) \sum_{\langle ij\rangle} \hat{\mathbf{S}}_i \cdot \hat{\mathbf{S}}_j + J_c \sum_{\langle\langle ij\rangle\rangle} \hat{\mathbf{S}}_i \cdot \hat{\mathbf{S}}_j + 4J_c \sum_{\langle ijkl\rangle} (\hat{Q}_{ijkl} + \hat{Q}_{iljk} - \hat{Q}_{ikjl}) + \frac{3J_c L}{4}. \tag{B5}$$

2. Rotating frame

The 120° Néel ordered state has a three-sublattice structure, as shown in Fig. 7. However, the introduction of a rotating frame [114–121] allows us to develop a one-sublattice spin-wave theory for the 120° Néel ordered state.

In terms of the spin operators in the rotating frame (X-Y-Z), the spin operators in the original frame (x-y-z) can be written as

$$\begin{aligned}
\hat{S}^x_i &= \cos\theta_i \hat{S}^X_i + \sin\theta_i \hat{S}^Z_i, \\
\hat{S}^y_i &= \hat{S}^Y_i, \\
\hat{S}^z_i &= \cos\theta_i \hat{S}^Z_i - \sin\theta_i \hat{S}^X_i,
\end{aligned} \tag{B6}$$

where $\theta_i = \mathbf{Q} \cdot \mathbf{r}_i$ with $\mathbf{Q} = (4\pi/3, 0)$ being a wave vector corresponding to the 120° order and $\mathbf{r}_i$ the position of site i. The inner product of spin operators is thus given by

$$\begin{aligned}
\hat{\mathbf{S}}_i \cdot \hat{\mathbf{S}}_j = {}& \hat{S}^Y_i \hat{S}^Y_j + \big(\hat{S}^Z_i \hat{S}^Z_j + \hat{S}^X_i \hat{S}^X_j\big) \cos\theta_{ij} \\
&+ \big(\hat{S}^Z_i \hat{S}^X_j - \hat{S}^X_i \hat{S}^Z_j\big) \sin\theta_{ij},
\end{aligned} \tag{B7}$$

where $\theta_{ij} = \theta_i - \theta_j$.

We assume that the spins are pointing along the Z axis of the rotating (X-Y-Z) frame. The Holstein-Primakoff transformation [122] for the spin operators in the rotating frame

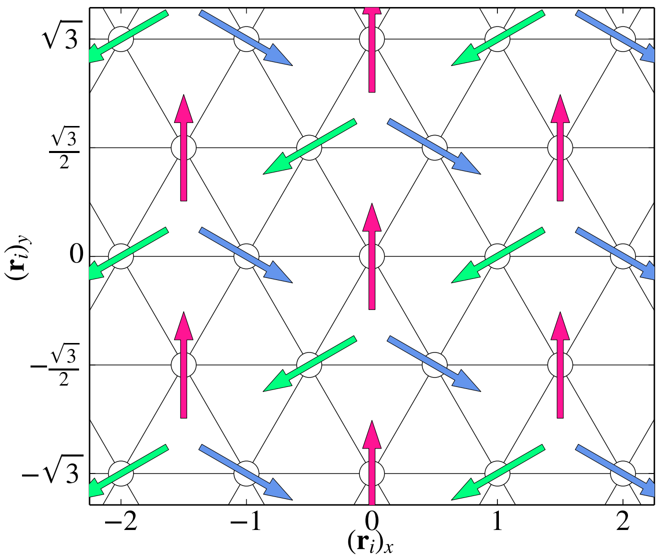

FIG. 7. Schematic figure of the 120° Néel ordered state on the triangular lattice. $(\mathbf{r}_i)_{x(y)}$ denotes the x (y) coordinate of $\mathbf{r}_i$.

results in

$$\begin{aligned}
\hat{S}_i^Z &= S - \hat{a}_i^\dagger \hat{a}_i,\\
\hat{S}_i^- &= \sqrt{2S}\hat{a}_i^\dagger\left(1 - \frac{\hat{a}_i^\dagger \hat{a}_i}{2S}\right)^{\frac{1}{2}},\\
\hat{S}_i^+ &= \sqrt{2S}\left(1 - \frac{\hat{a}_i^\dagger \hat{a}_i}{2S}\right)^{\frac{1}{2}}\hat{a}_i,
\end{aligned} \tag{B8}$$

where $\hat{S}_i^- = \hat{S}_i^X - \mathrm{i}\hat{S}_i^Y$, $\hat{S}_i^+ = (\hat{S}_i^-)^\dagger$, and $\hat{a}_i$ and $\hat{a}_i^\dagger$ are bosonic annihilation and creation operators, respectively, satisfying the canonical commutation relations $[\hat{a}_i, \hat{a}_j] = 0$ and $[\hat{a}_i, \hat{a}_j^\dagger] = \delta_{ij}$.

3. Linear spin-wave approximation

Up to the quadratic terms of the bosonic operators, the inner product of the spin operators is approximated as

$$\begin{aligned}
\hat{\mathbf{S}}_i \cdot \hat{\mathbf{S}}_j \approx\ & S^2 + S\cos\theta_{ij}(\hat{a}_i^\dagger \hat{a}_i + \hat{a}_j^\dagger \hat{a}_j)\\
&+ \frac{S}{2}(\cos\theta_{ij} + 1)(\hat{a}_i^\dagger \hat{a}_j + \hat{a}_j^\dagger \hat{a}_i)\\
&+ \frac{S}{2}(\cos\theta_{ij} - 1)(\hat{a}_i^\dagger \hat{a}_j^\dagger + \hat{a}_j \hat{a}_i).
\end{aligned} \tag{B9}$$

Notice that $\cos\theta_{ij} = -1/2$ for the nearest neighbors and $\cos\theta_{ij} = 1$ for next-nearest neighbors.

Similarly, $\hat{Q}_{ijkl}$ is approximated as

$$\begin{aligned}
\hat{Q}_{ijkl} \approx\ & \hat{S}_i^Z \hat{S}_j^Z \hat{S}_k^Z \hat{S}_l^Z \cos\theta_{ij}\cos\theta_{kl}\\
&+ \hat{S}_i^Z \hat{S}_j^Z \hat{S}_k^X \hat{S}_l^X \cos\theta_{ij}\cos\theta_{kl}\\
&+ \hat{S}_k^Z \hat{S}_l^Z \hat{S}_i^X \hat{S}_j^X \cos\theta_{ij}\cos\theta_{kl}\\
&+ \hat{S}_i^Z \hat{S}_j^Z \hat{S}_k^Y \hat{S}_l^Y \cos\theta_{ij}\\
&+ \hat{S}_k^Z \hat{S}_l^Z \hat{S}_i^Y \hat{S}_j^Y \cos\theta_{kl}\\
&+ \big(\hat{S}_i^Z \hat{S}_j^X - \hat{S}_i^X \hat{S}_j^Z\big)\big(\hat{S}_k^Z \hat{S}_l^X - \hat{S}_k^X \hat{S}_l^Z\big)\sin\theta_{ij}\sin\theta_{kl}\\
\approx\ & [S^4 - S^3(\hat{a}_i^\dagger \hat{a}_i + \hat{a}_j^\dagger \hat{a}_j + \hat{a}_k^\dagger \hat{a}_k + \hat{a}_l^\dagger \hat{a}_l)]\cos\theta_{ij}\cos\theta_{kl}\\
&+ \frac{S^3}{2}(\hat{a}_i^\dagger \hat{a}_j + \text{H.c.})\cos\theta_{kl}(\cos\theta_{ij} + 1)\\
&+ \frac{S^3}{2}(\hat{a}_k^\dagger \hat{a}_l + \text{H.c.})\cos\theta_{ij}(\cos\theta_{kl} + 1)\\
&+ \frac{S^3}{2}(\hat{a}_i^\dagger \hat{a}_j^\dagger + \text{H.c.})\cos\theta_{kl}(\cos\theta_{ij} - 1)\\
&+ \frac{S^3}{2}(\hat{a}_k^\dagger \hat{a}_l^\dagger + \text{H.c.})\cos\theta_{ij}(\cos\theta_{kl} - 1)\\
&+ \frac{S^3}{2}\sin\theta_{ij}\sin\theta_{kl}\\
&\times(\hat{a}_j^\dagger \hat{a}_l - \hat{a}_j^\dagger \hat{a}_k - \hat{a}_i^\dagger \hat{a}_l + \hat{a}_i^\dagger \hat{a}_k + \hat{a}_j^\dagger \hat{a}_l^\dagger\\
&-\hat{a}_j^\dagger \hat{a}_k^\dagger - \hat{a}_i^\dagger \hat{a}_l^\dagger + \hat{a}_i^\dagger \hat{a}_k^\dagger + \text{H.c.}).
\end{aligned} \tag{B10}$$

By substituting $\cos\theta_{ij} = \cos\theta_{kl} = \cos\theta_{il} = \cos\theta_{jk} = \cos\theta_{jl} = -1/2$, $\cos\theta_{ik} = 1$, $\sin\theta_{ij}\sin\theta_{kl} = -3/4$, $\sin\theta_{il}\sin\theta_{jk} = 3/4$, and $\sin\theta_{ik}\sin\theta_{jl} = 0$ for $\hat{Q}_{ijkl}$, $\hat{Q}_{iljk}$, and $\hat{Q}_{ikjl}$ in the last term of Eq. (B1), we find

$$\begin{aligned}
&\hat{Q}_{ijkl} + \hat{Q}_{iljk} - \hat{Q}_{ikjl}\\
&\quad\approx S^4 - S^3(\hat{a}_i^\dagger \hat{a}_i + \hat{a}_j^\dagger \hat{a}_j + \hat{a}_k^\dagger \hat{a}_k + \hat{a}_l^\dagger \hat{a}_l)\\
&\quad+ \frac{S^3}{4}(\hat{a}_i^\dagger \hat{a}_j + \hat{a}_k^\dagger \hat{a}_l + \hat{a}_i^\dagger \hat{a}_l + \hat{a}_j^\dagger \hat{a}_k\\
&\quad- \hat{a}_i^\dagger \hat{a}_k - 4\hat{a}_j^\dagger \hat{a}_l + \text{H.c.})\\
&\quad+ \frac{3S^3}{4}(\hat{a}_i^\dagger \hat{a}_j^\dagger + \hat{a}_k^\dagger \hat{a}_l^\dagger + \hat{a}_i^\dagger \hat{a}_l^\dagger + \hat{a}_j^\dagger \hat{a}_k^\dagger - \hat{a}_i^\dagger \hat{a}_k^\dagger + \text{H.c.}).
\end{aligned} \tag{B11}$$

Notice in Eq. (B11) that the subscript pair (i, k) contributes to the next-nearest-neighbor terms, while the others to the nearest-neighbor terms.

4. Spin-wave Hamiltonian

By substituting the approximations in Eqs. (B9) and (B11) into the Hamiltonian in Eq. (B5), and carefully evaluating the sum over all plaquettes, similarly in Eq. (B4), we obtain the spin-wave Hamiltonian

$$\begin{aligned}
\hat{H} &\approx \hat{H}_{\text{sw}}\\
&= E_{\text{sw}} + 3SA_0\sum_i \hat{a}_i^\dagger \hat{a}_i\\
&\quad+ \frac{S}{4}\left[A_1\sum_{\langle ij\rangle}(\hat{a}_i^\dagger \hat{a}_j + \hat{a}_j^\dagger \hat{a}_j) + A_2\sum_{\langle\langle ij\rangle\rangle}(\hat{a}_i^\dagger \hat{a}_j + \hat{a}_j^\dagger \hat{a}_j)\right]\\
&\quad- \frac{3S}{4}\left[B_1\sum_{\langle ij\rangle}(\hat{a}_i^\dagger \hat{a}_j^\dagger + \hat{a}_i \hat{a}_j) + B_2\sum_{\langle\langle ij\rangle\rangle}(\hat{a}_i^\dagger \hat{a}_j^\dagger + \hat{a}_i \hat{a}_j)\right],
\end{aligned} \tag{B12}$$

where

$$\begin{aligned}
A_0 &= J + 3J_{\text{c}} - 16S^2 J_{\text{c}},\\
A_1 &= J + 5J_{\text{c}},\\
A_2 &= 4(1 - S^2)J_{\text{c}},
\end{aligned}$$

$$\begin{aligned} B_1 &= J + 5J_c - 16S^2J_c, \\ B_2 &= 4S^2J_c, \end{aligned} \tag{B13}$$

and

$$E_{\text{sw}} = -\frac{3}{2}\left[(J + 3J_c - 8S^2J_c)S^2 - \frac{J_c}{2}\right]L. \tag{B14}$$

With the Fourier transformation of the bosonic operators $\hat{a}_i = \frac{1}{\sqrt{L}}\sum_{\mathbf{q}} \hat{a}_{\mathbf{q}} e^{i\mathbf{q}\cdot\mathbf{r}_i}$, $\hat{H}_{\text{sw}}$ in the momentum space is given by

$$\begin{aligned} \hat{H}_{\text{sw}} &= E_{\text{sw}} + \sum_{\mathbf{q}}\left[A(\mathbf{q})\hat{a}^\dagger_{\mathbf{q}}\hat{a}_{\mathbf{q}} - \frac{1}{2}B(\mathbf{q})(\hat{a}^\dagger_{\mathbf{q}}\hat{a}^\dagger_{-\mathbf{q}} + \hat{a}_{-\mathbf{q}}\hat{a}_{\mathbf{q}})\right] \\ &= E_{\text{sw}} - \frac{1}{2}\sum_{\mathbf{q}} A(\mathbf{q}) \\ &\quad + \frac{1}{2}\sum_{\mathbf{q}} (\hat{a}^\dagger_{\mathbf{q}} \quad \hat{a}_{-\mathbf{q}}) \begin{pmatrix} A(\mathbf{q}) & -B(\mathbf{q}) \\ -B(\mathbf{q}) & A(\mathbf{q}) \end{pmatrix} \begin{pmatrix} \hat{a}_{\mathbf{q}} \\ \hat{a}^\dagger_{-\mathbf{q}} \end{pmatrix}, \end{aligned} \tag{B15}$$

where

$$A(\mathbf{q}) = 3S\left[A_0 + \frac{A_1}{2}\gamma(\mathbf{q}) + \frac{A_2}{2}\gamma'(\mathbf{q})\right], \tag{B16}$$

$$B(\mathbf{q}) = \frac{9S}{2}[B_1\gamma(\mathbf{q}) + B_2\gamma'(\mathbf{q})], \tag{B17}$$

$\gamma(\mathbf{q}) = \frac{1}{6}\sum_{i=1}^{6} e^{i\mathbf{q}\cdot\boldsymbol{\delta}_i}$, and $\gamma'(\mathbf{q}) = \frac{1}{6}\sum_{i=1}^{6} e^{i\mathbf{q}\cdot\boldsymbol{\delta}'_i}$ with $\boldsymbol{\delta}_i$ ($\boldsymbol{\delta}'_i$) being the vectors connecting the nearest (next-nearest) neighbors.

5. Spin-wave dispersion

We now introduce a Bogoliubov transformation

$$\begin{pmatrix} \hat{a}_{\mathbf{q}} \\ \hat{a}^\dagger_{-\mathbf{q}} \end{pmatrix} = \begin{pmatrix} u_{\mathbf{q}} & v_{\mathbf{q}} \\ v_{\mathbf{q}} & u_{\mathbf{q}} \end{pmatrix} \begin{pmatrix} \hat{b}_{\mathbf{q}} \\ \hat{b}^\dagger_{-\mathbf{q}} \end{pmatrix} \tag{B18}$$

under the condition $u^2_{\mathbf{q}} - v^2_{\mathbf{q}} = 1$ and thus the new operators $\hat{b}_{\mathbf{q}}$ and $\hat{b}^\dagger_{\mathbf{q}}$ obey the canonical bosonic commutation relations. If $u_{\mathbf{q}}$ and $v_{\mathbf{q}}$ are chosen to satisfy $u^2_{\mathbf{q}} + v^2_{\mathbf{q}} = A(\mathbf{q})/\Omega(\mathbf{q})$ and $2u_{\mathbf{q}}v_{\mathbf{q}} = B(\mathbf{q})/\Omega(\mathbf{q})$ with

$$\Omega(\mathbf{q}) = \sqrt{A(\mathbf{q})^2 - B(\mathbf{q})^2}, \tag{B19}$$

then the spin-wave Hamiltonian is given by

$$\hat{H}_{\text{sw}} = E_{\text{sw}} - \frac{1}{2}\sum_{\mathbf{q}} A(\mathbf{q}) + \sum_{\mathbf{q}} \Omega(\mathbf{q})\left(\hat{b}^\dagger_{\mathbf{q}}\hat{b}_{\mathbf{q}} + \frac{1}{2}\right), \tag{B20}$$

where $\Omega(\mathbf{q})$ is the spin-wave dispersion.

Figure 8(a) shows the $S = 1/2$ spin-wave dispersion $\Omega(\mathbf{q})$ for several values of J_c/J along the high symmetric momentum direction Γ–K–M–Γ, where $\Gamma = (0, 0)$, $K = (4\pi/3, 0)$, and $M = (\pi, \pi/\sqrt{3})$ (also see Fig. 2). The zero modes at the Γ, K, and K' points are preserved because $A(\Gamma) = B(\Gamma) = \frac{9S}{2}(J + 5J_c - 12S^2J_c)$ and $A(\pm K) = -B(\pm K) = \frac{9S}{4}(J + 5J_c - 24S^2J_c)$. The excitation energy at the M point is given by

$$\begin{aligned} \Omega(M) &= 2S\sqrt{[J - (3 + 28S^2)J_c][J + (3 - 16S^2)J_c]} \\ &= \sqrt{(J - 10J_c)(J - J_c)}, \end{aligned} \tag{B21}$$

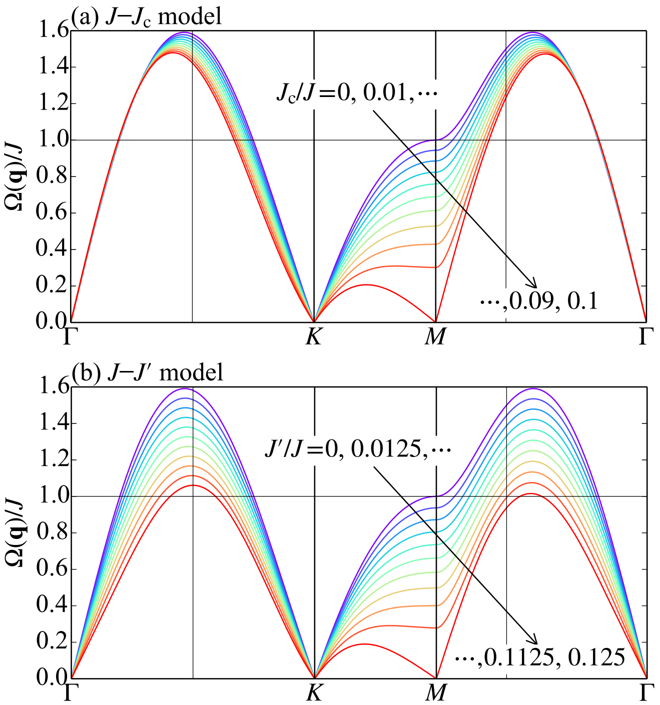

FIG. 8. Linear spin-wave dispersions for (a) the J-J_c model and (b) the J-J' model with several J_c/J and J'/J values indicated, respectively, in the figures. The horizontal axis is momentum $\mathbf{q}$ along the Γ–K–M–Γ points in the (nonmagnetic) Brillouin zone, where $\Gamma = (0, 0)$, $K = (4\pi/3, 0)$, and $M = (\pi, \pi/\sqrt{3})$. Thin vertical lines indicate the magnetic Brillouin-zone boundaries corresponding to the 120° Néel order. The horizontal line at $\Omega(\mathbf{q})/J = 1$ indicates the spin-wave excitation energy at M point in the purely triangular case with $J_c = J' = 0$.

where the second line is for $S = 1/2$. It is found that the spin-wave excitation energy along the K–M line, especially at the M point, reduces drastically with increasing J_c/J, and eventually becomes zero when $J_c/J = 0.1$, implying instability of the 120° Néel order. On the other hand, the spin-wave velocity around the Γ point remains the same and the highest spin-wave excitation energy is kept around $1.5J$ as J_c/J is increased.

For a comparison, Fig. 8(b) shows the $S = 1/2$ linear spin-wave dispersion $\Omega(\mathbf{q})$ for the J-J' model defined as

$$\hat{H}_{JJ'} = J\sum_{\langle ij\rangle} \hat{\mathbf{S}}_i \cdot \hat{\mathbf{S}}_j + J'\sum_{\langle\langle ij\rangle\rangle} \hat{\mathbf{S}}_i \cdot \hat{\mathbf{S}}_j \tag{B22}$$

with J' being the next-nearest-neighbor exchange interaction. The linear spin-wave dispersion for this model can be obtained by replacing A_0, A_1, A_2, B_1, and B_2 in Eqs. (B16) and (B17) with $\tilde{A}_0$, $\tilde{A}_1$, $\tilde{A}_2$, $\tilde{B}_1$, and $\tilde{B}_2$, where

$$\begin{aligned} \tilde{A}_0 &= J - 2J', \\ \tilde{A}_1 &= J, \quad \tilde{A}_2 = 4J', \\ \tilde{B}_1 &= J, \quad \tilde{B}_2 = 0. \end{aligned} \tag{B23}$$

Again the zero modes at the Γ, K, and K' points are preserved with increasing J'/J. The excitation energy at the M point is given by

$$\Omega(M) = 2S\sqrt{(J-8J')(J-2J')} = \sqrt{(J-8J')(J-2J')}. \quad \text{(B24)}$$

Similarly to the J-J_c model, the spin-wave excitation energy at the M point reduces most significantly with increasing J'/J, and eventually becomes zero when $J'/J = 1/8$. However, differently from the J-J_c model, the spin-wave velocity around the Γ point reduces and the highest spin-wave excitation energy is also reduced from $\sim 1.6J$ to $\sim 1.05J$ as J'/J is increased. A similar dependence of the excitation energy on the interaction parameter J' has been found also in the square lattice with the linear spin-wave theory [42].

The spin-wave excitation has two characteristic energy scales. One is the maxima of $\Omega(\mathbf{q})$ and the other is the saddle points, minima, and nearly flat dispersion of $\Omega(\mathbf{q})$ at and around the M and equivalent points. The comparison of the spin-wave dispersions suggests that, although both J_c and J' can increase the separation of the two energy scales, the more significant separation may appear in the J-J_c model rather than in the J-J' model. Note however that analytical and numerical studies beyond the linear spin-wave theory [13,123,124] have shown a strong renormalization of the magnon excitation energy as compared to the spin-wave theory for the pure triangular-lattice case with $J_c = J' = 0$.

Finally, we note that the spin-wave analysis captures the magnon excitations but not nonmagnetic ones. Indeed, we were not able to find the double-peak structure of the specific heat within the spin-wave analysis. This implies that the nonmagnetic excitations beyond the simple magnon excitations might be essential to understand the characteristic double-peak structure of the specific heat found here in the finite-temperature Lanczos calculations.

---

[1] P. Anderson, Mater. Res. Bull. **8**, 153 (1973).
[2] P. Fazekas and P. W. Anderson, Philos. Mag.: A J. Theor. Exp. Appl. Phys. **30**, 423 (1974).
[3] B. Bernu, C. Lhuillier, and L. Pierre, Phys. Rev. Lett. **69**, 2590 (1992).
[4] B. Bernu, P. Lecheminant, C. Lhuillier, and L. Pierre, Phys. Rev. B **50**, 10048 (1994).
[5] G. Misguich, C. Lhuillier, B. Bernu, and C. Waldtmann, Phys. Rev. B **60**, 1064 (1999).
[6] L. Capriotti, A. E. Trumper, and S. Sorella, Phys. Rev. Lett. **82**, 3899 (1999).
[7] S. Yunoki and S. Sorella, Phys. Rev. B **74**, 014408 (2006).
[8] S. R. White and A. L. Chernyshev, Phys. Rev. Lett. **99**, 127004 (2007).
[9] P. Lecheminant, B. Bernu, C. Lhuillier, and L. Pierre, Phys. Rev. B **52**, 6647 (1995).
[10] L. O. Manuel and H. A. Ceccatto, Phys. Rev. B **60**, 9489 (1999).
[11] R. Kaneko, S. Morita, and M. Imada, J. Phys. Soc. Jpn. **83**, 093707 (2014).
[12] Y. Iqbal, W.-J. Hu, R. Thomale, D. Poilblanc, and F. Becca, Phys. Rev. B **93**, 144411 (2016).
[13] F. Ferrari and F. Becca, Phys. Rev. X **9**, 031026 (2019).
[14] G. Misguich, B. Bernu, C. Lhuillier, and C. Waldtmann, Phys. Rev. Lett. **81**, 1098 (1998).
[15] O. I. Motrunich, Phys. Rev. B **72**, 045105 (2005).
[16] R. V. Mishmash, J. R. Garrison, S. Bieri, and C. Xu, Phys. Rev. Lett. **111**, 157203 (2013).
[17] C. J. Calzado and J.-P. Malrieu, Phys. Rev. B **69**, 094435 (2004).
[18] K. Tanaka, Y. Yokoyama, and C. Hotta, J. Phys. Soc. Jpn. **87**, 023702 (2018).
[19] H. Morita, S. Watanabe, and M. Imada, J. Phys. Soc. Jpn. **71**, 2109 (2002).
[20] T. Koretsune, Y. Motome, and A. Furusaki, J. Phys. Soc. Jpn. **76**, 074719 (2007).
[21] P. Sahebsara and D. Sénéchal, Phys. Rev. Lett. **100**, 136402 (2008).
[22] T. Yoshioka, A. Koga, and N. Kawakami, Phys. Rev. Lett. **103**, 036401 (2009).
[23] L. F. Tocchio, H. Feldner, F. Becca, R. Valentí, and C. Gros, Phys. Rev. B **87**, 035143 (2013).
[24] A. Yamada, Phys. Rev. B **89**, 195108 (2014).
[25] M. Laubach, R. Thomale, C. Platt, W. Hanke, and G. Li, Phys. Rev. B **91**, 245125 (2015).
[26] K. Misumi, T. Kaneko, and Y. Ohta, Phys. Rev. B **95**, 075124 (2017).
[27] T. Shirakawa, T. Tohyama, J. Kokalj, S. Sota, and S. Yunoki, Phys. Rev. B **96**, 205130 (2017).
[28] A. Szasz, J. Motruk, M. P. Zaletel, and J. E. Moore, Phys. Rev. X **10**, 021042 (2020).
[29] J. Skolimowski, Y. Gerasimenko, and R. Žitko, Phys. Rev. Lett. **122**, 036802 (2019).
[30] A. K. McMahan and J. W. Wilkins, Phys. Rev. Lett. **35**, 376 (1975).
[31] J. H. Hetherington and F. D. C. Willard, Phys. Rev. Lett. **35**, 1442 (1975).
[32] M. Roger, J. M. Delrieu, and J. H. Hetherington, Phys. Rev. Lett. **45**, 137 (1980).
[33] K. Yosida, Prog. Theor. Phys. Suppl. **69**, 475 (1980).
[34] D. M. Ceperley and G. Jacucci, Phys. Rev. Lett. **58**, 1648 (1987).
[35] M. Roger, J. Low Temp. Phys. **162**, 625 (2011).
[36] L. Cândido, G.-Q. Hai, and D. M. Ceperley, Phys. Rev. B **84**, 064515 (2011).
[37] K. Yosida and S. Inagaki, J. Phys. Soc. Jpn. **50**, 3268 (1981).
[38] J. Lorenzana, J. Eroles, and S. Sorella, Phys. Rev. Lett. **83**, 5122 (1999).
[39] R. Coldea, S. M. Hayden, G. Aeppli, T. G. Perring, C. D. Frost, T. E. Mason, S.-W. Cheong, and Z. Fisk, Phys. Rev. Lett. **86**, 5377 (2001).
[40] A. A. Katanin and A. P. Kampf, Phys. Rev. B **66**, 100403(R) (2002).
[41] N. S. Headings, S. M. Hayden, R. Coldea, and T. G. Perring, Phys. Rev. Lett. **105**, 247001 (2010).

[42] M. S. Rutonjski, M. V. Pavkov-Hrvojević, and M. B. Berović, Int. J. Mod. Phys. B **30**, 1550251 (2016).

[43] S. Yamamoto and Y. Noriki, Phys. Rev. B **99**, 094412 (2019).

[44] K. T. Law and P. A. Lee, Proc. Natl. Acad. Sci. **114**, 6996 (2017).

[45] W.-Y. He, X. Y. Xu, G. Chen, K. T. Law, and P. A. Lee, Phys. Rev. Lett. **121**, 046401 (2018).

[46] Y. Shimizu, K. Miyagawa, K. Kanoda, M. Maesato, and G. Saito, Phys. Rev. Lett. **91**, 107001 (2003).

[47] Y. Kurosaki, Y. Shimizu, K. Miyagawa, K. Kanoda, and G. Saito, Phys. Rev. Lett. **95**, 177001 (2005).

[48] R. S. Manna, M. de Souza, A. Brühl, J. A. Schlueter, and M. Lang, Phys. Rev. Lett. **104**, 016403 (2010).

[49] T. Itou, A. Oyamada, S. Maegawa, M. Tamura, and R. Kato, Phys. Rev. B **77**, 104413 (2008).

[50] M. Yamashita, N. Nakata, Y. Senshu, M. Nagata, H. M. Yamamoto, R. Kato, T. Shibauchi, and Y. Matsuda, Science **328**, 1246 (2010).

[51] P. Fazekas and E. Tosatti, Philos. Mag. B **39**, 229 (1979).

[52] M. Klanjsek, A. Zorko, R. Zitko, J. Mravlje, Z. Jaglicic, P. Biswas, P. Prelovsek, D. Mihailovic, and D. Arcon, Nat. Phys. **13**, 1130 (2017).

[53] M. Roger, Phys. Rev. B **30**, 6432 (1984).

[54] M. Roger, Phys. Rev. Lett. **64**, 297 (1990).

[55] K. Ishida, M. Morishita, K. Yawata, and H. Fukuyama, Phys. Rev. Lett. **79**, 3451 (1997).

[56] M. Roger, C. Bäuerle, Y. M. Bunkov, A.-S. Chen, and H. Godfrin, Phys. Rev. Lett. **80**, 1308 (1998).

[57] T. Momoi, H. Sakamoto, and K. Kubo, Phys. Rev. B **59**, 9491 (1999).

[58] T. Momoi, P. Sindzingre, and N. Shannon, Phys. Rev. Lett. **97**, 257204 (2006).

[59] H. Fukuyama, J. Phys. Soc. Jpn. **77**, 111013 (2008).

[60] Y. Fuseya and M. Ogata, J. Phys. Soc. Jpn. **78**, 013601 (2009).

[61] K. Seki, T. Shirakawa, and Y. Ohta, Phys. Rev. B **79**, 024303 (2009).

[62] T. Momoi, P. Sindzingre, and K. Kubo, Phys. Rev. Lett. **108**, 057206 (2012).

[63] S. Moroni and M. Boninsegni, Phys. Rev. B **99**, 195441 (2019).

[64] W. LiMing, G. Misguich, P. Sindzingre, and C. Lhuillier, Phys. Rev. B **62**, 6372 (2000).

[65] R. Kato, Bull. Chem. Soc. Jpn. **87**, 355 (2014).

[66] R. Rawl, L. Ge, H. Agrawal, Y. Kamiya, C. R. Dela Cruz, N. P. Butch, X. F. Sun, M. Lee, E. S. Choi, J. Oitmaa, C. D. Batista, M. Mourigal, H. D. Zhou, and J. Ma, Phys. Rev. B **95**, 060412(R) (2017).

[67] Y. Cui, J. Dai, P. Zhou, P. S. Wang, T. R. Li, W. H. Song, J. C. Wang, L. Ma, Z. Zhang, S. Y. Li, G. M. Luke, B. Normand, T. Xiang, and W. Yu, Phys. Rev. Materials **2**, 044403 (2018).

[68] P. Prelovšek, K. Morita, T. Tohyama, and J. Herbrych, Phys. Rev. Research **2**, 023024 (2020).

[69] K. Morita and T. Tohyama, Phys. Rev. Research **2**, 013205 (2020).

[70] J. Jaklič and P. Prelovšek, Phys. Rev. B **49**, 5065 (1994).

[71] J. Jaklič and P. Prelovšek, Adv. Phys. **49**, 1 (2000).

[72] P. Prelovšek and J. Bonča, Ground state and finite temperature lanczos methods, in *Strongly Correlated Systems: Numerical Methods*, edited by A. Avella and F. Mancini (Springer, Berlin, Heidelberg, 2013), pp. 1–30.

[73] T. Iitaka and T. Ebisuzaki, Phys. Rev. E **69**, 057701 (2004).

[74] A. Weiße, G. Wellein, A. Alvermann, and H. Fehske, Rev. Mod. Phys. **78**, 275 (2006).

[75] D. A. Drabold and O. F. Sankey, Phys. Rev. Lett. **70**, 3631 (1993).

[76] F. Chatelin, *Valeurs Propres de Matrices* (Masson, Paris, 1988), translation by M. Iri and Y. Iri (Springer, Tokyo, 2003).

[77] T. Shirakawa and S. Yunoki, Phys. Rev. B **90**, 195109 (2014).

[78] A. Allerdt, C. A. Büsser, G. B. Martins, and A. E. Feiguin, Phys. Rev. B **91**, 085101 (2015).

[79] K. Seki, T. Shirakawa, and S. Yunoki, Phys. Rev. B **98**, 205114 (2018).

[80] M. Aichhorn, M. Daghofer, H. G. Evertz, and W. von der Linden, Phys. Rev. B **67**, 161103(R) (2003).

[81] J. Schnack, J. Schulenburg, and J. Richter, Phys. Rev. B **98**, 094423 (2018).

[82] J. Schnack, J. Richter, and R. Steinigeweg, Phys. Rev. Res. **2**, 013186 (2020).

[83] S. Sugiura and A. Shimizu, Phys. Rev. Lett. **111**, 010401 (2013).

[84] H. Nishida, R. Fujiuchi, K. Sugimoto, and Y. Ohta, J. Phys. Soc. Jpn. **89**, 023702 (2020).

[85] H. Tal-Ezer and R. Kosloff, J. Chem. Phys. **81**, 3967 (1984).

[86] L.-W. Wang, Phys. Rev. B **49**, 10154 (1994).

[87] L.-W. Wang and A. Zunger, Phys. Rev. Lett. **73**, 1039 (1994).

[88] T. Iitaka, Phys. Rev. E **49**, 4684 (1994).

[89] A. Vijay and H. Metiu, J. Chem. Phys. **116**, 60 (2002).

[90] T. Iitaka and T. Ebisuzaki, Phys. Rev. Lett. **90**, 047203 (2003).

[91] M. Machida, T. Iitaka, and S. Miyashita, J. Phys. Soc. Jpn. **74**, 107 (2005).

[92] A. Weiße and H. Fehske, *Computational Many-Particle Physics*, edited by H. Fehske, R. Schneider, and A. Weiße, Lect. Notes Phys. 739 (Springer, Berlin, Heidelberg, 2008), Chap. 19, pp. 545–577.

[93] K. Seki, Y. Otsuka, S. Yunoki, and S. Sorella, Phys. Rev. B **99**, 125145 (2019).

[94] J. M. Deutsch, Phys. Rev. A **43**, 2046 (1991).

[95] M. Srednicki, Phys. Rev. E **50**, 888 (1994).

[96] I. Rousochatzakis, S. Kourtis, J. Knolle, R. Moessner, and N. B. Perkins, Phys. Rev. B **100**, 045117 (2019).

[97] P. Prelovšek and J. Kokalj, Phys. Rev. B **101**, 075105 (2020).

[98] See Supplemental Material at http://link.aps.org/supplemental/10.1103/PhysRevB.101.235115 for details on the finite-size effects.

[99] P. Prelovšek and J. Kokalj, Phys. Rev. B **98**, 035107 (2018).

[100] B.-B. Chen, L. Chen, Z. Chen, W. Li, and A. Weichselbaum, Phys. Rev. X **8**, 031082 (2018).

[101] L. Chen, D.-W. Qu, H. Li, B.-B. Chen, S.-S. Gong, J. von Delft, A. Weichselbaum, and W. Li, Phys. Rev. B **99**, 140404(R) (2019).

[102] B. Bernu and G. Misguich, Phys. Rev. B **63**, 134409 (2001).

[103] H.-Y. Yang, A. M. Läuchli, F. Mila, and K. P. Schmidt, Phys. Rev. Lett. **105**, 267204 (2010).

[104] P. Lecheminant, B. Bernu, C. Lhuillier, L. Pierre, and P. Sindzingre, Phys. Rev. B **56**, 2521 (1997).

[105] C. Waldtmann, H.-U. Everts, B. Bernu, C. Lhuillier, P. Sindzingre, P. Lecheminant, and L. Pierre, Eur. Phys. J. B **2**, 501 (1998).

[106] T. Shimokawa and H. Kawamura, J. Phys. Soc. Jpn. **85**, 113702 (2016).

[107] Y. Yamaji, T. Suzuki, T. Yamada, S.-i. Suga, N. Kawashima, and M. Imada, Phys. Rev. B **93**, 174425 (2016).

[108] N. D. Mermin and H. Wagner, Phys. Rev. Lett. **17**, 1133 (1966).

[109] M. Kratochvilova, A. D. Hillier, A. R. Wildes, L. Wang, S.-W. Cheong, and J.-G. Park, npj Quantum Mater. **2**, 42 (2017).

[110] A. Ribak, I. Silber, C. Baines, K. Chashka, Z. Salman, Y. Dagan, and A. Kanigel, Phys. Rev. B **96**, 195131 (2017).

[111] H. Murayama, Y. Sato, T. Taniguchi, R. Kurihara, X. Z. Xing, W. Huang, S. Kasahara, Y. Kasahara, I. Kimchi, M. Yoshida, Y. Iwasa, Y. Mizukami, T. Shibauchi, M. Konczykowski, and Y. Matsuda, Phys. Rev. Research **2**, 013099 (2020).

[112] D. S. Greywall and P. A. Busch, Phys. Rev. Lett. **62**, 1868 (1989).

[113] H. Q. Lin, Phys. Rev. B **42**, 6561 (1990).

[114] T. Oguchi, H. Nishimori, and Y. Taguchi, J. Phys. Soc. Jpn. **54**, 4494 (1985).

[115] S. J. Miyake, Prog. Theor. Phys. **74**, 468 (1985).

[116] P. W. Leung and K. J. Runge, Phys. Rev. B **47**, 5861 (1993).

[117] T. Ohyama and H. Shiba, J. Phys. Soc. Jpn. **62**, 3277 (1993).

[118] R. Deutscher and H. U. Everts, Z. Phys. B Condens. Matter **93**, 77 (1993).

[119] A. E. Trumper, L. Capriotti, and S. Sorella, Phys. Rev. B **61**, 11529 (2000).

[120] A. L. Chernyshev and M. E. Zhitomirsky, Phys. Rev. B **79**, 144416 (2009).

[121] M. E. Zhitomirsky and A. L. Chernyshev, Rev. Mod. Phys. **85**, 219 (2013).

[122] T. Holstein and H. Primakoff, Phys. Rev. **58**, 1098 (1940).

[123] W. Zheng, J. O. Fjærestad, R. R. P. Singh, R. H. McKenzie, and R. Coldea, Phys. Rev. B **74**, 224420 (2006).

[124] E. A. Ghioldi, A. Mezio, L. O. Manuel, R. R. P. Singh, J. Oitmaa, and A. E. Trumper, Phys. Rev. B **91**, 134423 (2015).